

The Galactic neutron star population I - an extragalactic view of the Milky Way and the implications for fast radio bursts

A. A. Chrimes,^{1*} A. J. Levan^{1,2}, P. J. Groot^{1,3,4}, J. D. Lyman² and G. Nelemans^{1,5,6}

¹*Department of Astrophysics/IMAPP, Radboud University Nijmegen, P.O. Box 9010, 6500 GL Nijmegen, The Netherlands*

²*Department of Physics, University of Warwick, Coventry CV4 7AL, UK*

³*Inter-University Institute for Data Intensive Astronomy, Department of Astronomy, University of Cape Town, Private Bag X3, Rondebosch 7701, South Africa*

⁴*South African Astronomical Observatory, P.O. Box 9, 7935 Observatory, South Africa*

⁵*Institute for Astronomy, KU Leuven, Leuven, Belgium*

⁶*SRON, Netherlands Institute for Space Research, Sorbonnelaan 2, NL-3584 CA Utrecht, The Netherlands*

Accepted XXX. Received YYY; in original form ZZZ

ABSTRACT

A key tool astronomers have to investigate the nature of extragalactic transients is their position on their host galaxies. Galactocentric offsets, enclosed fluxes and the fraction of light statistic are widely used at different wavelengths to help infer the nature of transient progenitors. Motivated by the proposed link between magnetars and fast radio bursts (FRBs), we create a face-on image of the Milky Way using best estimates of its size, structure and colour. We place Galactic magnetars, pulsars and X-ray binaries on this image, using the available distance information. Galactocentric offsets, enclosed fluxes and fraction of light distributions are compared to extragalactic transient samples. We find that FRBs are located on their hosts in a manner consistent with Galactic neutron stars on the Milky Way’s light, although we cannot determine which specific population is the best match. The Galactic distributions are consistent with other classes of extragalactic transient much less often, across the range of comparisons made. We demonstrate that the fraction of light method should be carefully used in galaxies with multiple components, and when comparing data with different redshift distributions and spatial resolutions. Star forming region offsets of a few hundred parsec are found to be typical of young neutron stars in the Milky Way, and therefore FRB offsets of this size do not preclude a magnetar origin, although the interpretation of these offsets is currently unclear. Overall, our results provide further support for FRB models invoking isolated young neutron stars, or binaries containing a neutron star.

Key words: stars: neutron – stars: magnetars – transients: fast radio bursts – supernovae: general – Galaxy: structure

1 INTRODUCTION

Several classes of astrophysical transients are associated with neutron stars, ranging from their formation in core-collapse supernovae to their mergers in short γ -ray bursts (GRBs). Magnetars are a subset of neutron stars (Duncan & Thompson 1992), distinguished by their extreme magnetic fields (10^{14} - 10^{15} G), high radio/X-ray/ γ -ray luminosities despite spin-down luminosities comparable to pulsars (Thompson & Duncan 1996; Kouveliotou et al. 1998), and young characteristic ages of $\sim 10^3$ - 10^5 yrs (Olausen & Kaspi 2014). Magnetars are observed in the Milky Way and Magellanic clouds as soft γ repeaters (SGRs, Mazets et al. 1979a,b) and anomalous X-ray pulsars (Fahlman & Gregory 1981), detectable primarily through their high energy flares, and in some cases persistent emission (Olausen & Kaspi 2014). Giant magnetar flares, detectable at extragalactic distances, have been identified as an alternative origin for some short GRBs (Hurley et al. 2005; Ofek et al. 2006, 2008; Svinikin et al. 2021; Burns et al. 2021). Magnetars have also been invoked as central engines in superluminous supernovae (Kasen & Bildsten 2010;

Woosley 2010) and GRBs (Metzger et al. 2008, 2011). More recently, they have become a promising explanation for the fast radio burst (FRB) phenomenon.

This paper is partly motivated by the FRB-magnetar connection, following the detection of FRB-like bursts from the Galactic magnetar SGR 1935+2154 (hereafter SGR 1935, Bochenek et al. 2020b; CHIME/FRB Collaboration et al. 2020). Although the SGR 1935 bursts are fainter than extragalactic FRBs, they are orders of magnitude brighter than other radio transients with comparable frequencies and millisecond durations (e.g. pulsar pulses, Keane 2018). Even before this detection, magnetar flaring was a leading theory among the dozens offered to explain FRBs (Platts et al. 2019)¹. See also Chatterjee (2020), Baring et al. (2020), Xiao et al. (2021) and Zhang (2020) for reviews. Despite this association, there are still open questions around the relationship between the X-ray/ γ -ray and radio emission (Katz 2016; Lin et al. 2020; De et al. 2020a; Tavani et al. 2021; Ridnaia et al. 2021; Li et al. 2021; Bailes et al. 2021; Verrecchia et al. 2021). It is unclear if all FRBs repeat, or if there are two distinct populations of single and repeating events, and the nature

* E-mail: a.chrimes@astro.ru.nl

¹ frbtheorycat.org/index.php/Main_Page

of the periodicity seen in repeating FRBs remains to be understood (Beniamini et al. 2020; Li & Zanazzi 2021).

If we assume that FRBs are caused by giant magnetar flares, and that SGR 1935 produces FRBs, then we must conclude that the Milky Way is an FRB host galaxy. If we also assume that all magnetars are capable of producing FRBs, then it follows that the distribution of FRBs on their host galaxies should match the distribution of magnetars on the Milky Way, at least for morphologically similar spiral galaxies. FRB sample size increases have led to more host identifications (Eftekhari & Berger 2017; Heintz et al. 2020)², and consequently, population studies of these hosts have now begun.

One way to study transient hosts is through their spectral energy distributions (SED), from which SED fitting can be used to infer the constituent stellar populations. Such work has found that FRB hosts span a range of masses and star formation rates, and correspondingly, morphological types. The mean stellar mass is around $\sim 10^{10} M_{\odot}$, and star formation rates are typically moderate $\sim 0.1 - 1 M_{\odot} \text{yr}^{-1}$ (Li & Zhang 2020; Bhandari et al. 2020; Heintz et al. 2020), comparable to the Milky Way. These properties disfavour very massive stellar progenitors, such as those of superluminous supernovae (SLSNe) and long GRBs, but are consistent with regular core-collapse supernova (CCSN) hosts.

The projected offset of transients from their host centre is another commonly used measure. At its most basic level, galaxies tend to have star formation rate gradients such that more star formation occurs towards the centre (neglecting metallicity effects and morphological differences). Furthermore, large offsets can provide insight into natal kicks, most prominently seen in short GRBs (Fong et al. 2010; Church et al. 2011; Tunnicliffe et al. 2014). Heintz et al. (2020) and Mannings et al. (2020) measure the physical offsets δr of FRBs from their hosts, and also the normalised offsets $\delta r/r_e$, where r_e is the half-light radius. Using the normalised offset accounts for different radial intensity profiles (for example, the underlying stellar mass at a given offset can be different in two otherwise identical galaxies, if their physical size and compactness differ). Heintz et al. (2020) and Mannings et al. (2020) find that CCSNe, SGRBs and type Ia SNe are the most consistent with FRB offsets.

In addition to global host offsets, a limited number of studies have been able to resolve the offset of FRBs from star forming regions within their hosts. Bassa et al. (2017) report that FRB 121102 (specifically, an associated persistent radio source) is encompassed by a star forming region within its host. Tendulkar et al. (2021) meanwhile find that FRB 180916B lies 250 pc from the centre of a nearby star forming region, and concluded that this is inconsistent with a magnetar origin, assuming kick velocities $< 750 \text{ km s}^{-1}$ and active lifetimes of $< 10 \text{ kyr}$. FRB 190608 is coincident with a bright knot of star formation in its host (Chittidi et al. 2020), but the uncertainty in the localisation of this FRB means that the offset from the edge of this region can only be constrained to less than $\sim 500 \text{ pc}$ (1σ uncertainty).

Another metric is the fraction of light (F_{light} , Fruchter et al. 2006). This technique ranks host-associated pixels and normalises their cumulative distribution, such that the brightest pixel on a galaxy is assigned the value 1, representing the cumulative fraction of total host flux ‘below’ that pixel. Unbiased tracers of light sample F_{light} values uniformly, whereas biased datasets over/under sample from brighter/fainter pixels. Different wavelengths are used to probe different stellar populations: shorter, UV/blue bands trace young stars and thus star formation, IR/red bands better trace older stars and stellar

mass. Mannings et al. (2020) compute F_{light} for 8 FRB hosts using UVIS and IR *Hubble Space Telescope*/WFC3 data. They compare to other transients, finding that type Ia SNe and SGRBs are the best match, but noting that the uncertainties are large. Nevertheless, this result suggests a stellar-mass tracing progenitor.

An intermediate method between offsets and F_{light} is to measure the enclosed fraction of the total galaxy flux within the galactocentric radius of the transient (James & Anderson 2006; Anderson & James 2009; Anderson et al. 2015a; Audcent-Ross et al. 2020). A cumulative distribution of the fractional enclosed fluxes will produce a 1:1 relation if the transient traces the light. Mannings et al. (2020) calculate this distribution for 8 FRBs on their hosts in the IR, again finding consistency with a stellar mass tracing progenitor.

As magnetars have been suggested as both the source of FRBs, and as the central engines/remnants of SLSNe and GRBs, there have been several targeted radio searches at the locations of recently (i.e. in the last few decades) observed transients. Searches of this nature have yet to detect an FRB (Metzger et al. 2017; Mondal et al. 2020; Hilmarsson et al. 2020; Palliyaguru et al. 2021), but deep optical searches have been able to rule out an association between FRBs and SLSNe/bright SNe Ia, GRB afterglows and tidal disruption events, on timescales of 1 day to 1 year post-burst (Nuñez et al. 2021).

A final method to explore the nature of FRB progenitors is to compare their redshift distribution to the cosmic star formation rate (SFR) history. FRB population synthesis has again found conflicting results, with some work finding that their rate is consistent with the SFR (and therefore magnetar production, Gardenier & van Leeuwen 2020; James et al. 2021), and others claiming that they better trace stellar mass (Luo et al. 2020)

As can be seen from this overview of host populations, offsets (host level and resolved), F_{light} , targeted searches for new FRB sources, and redshift distribution studies, the sole origin of FRBs in giant magnetar flares is still far from certain. Indeed, these results have led to conflicting interpretations over whether magnetars can explain all FRBs (Bochenek et al. 2020a; Safarzadeh et al. 2020), and if so, what the progenitor channels should be (Margalit et al. 2019, 2020). Our comparison of magnetar (and other neutron star) positions in the Milky Way, versus FRBs locations within their hosts, is therefore a valuable alternative diagnostic.

The aims of this paper require the ability to map both the Milky Way itself, and the neutron star populations within in. Galactic magnetars have been studied in detail, in terms of their distances, activity, magnetic fields, ages and more (Olausen & Kaspi 2014; Beniamini et al. 2019); pulsar (Manchester et al. 2005; Yao et al. 2017) and X-ray binary (XRB) catalogues are also maintained (Kretschmar et al. 2019; Sazonov et al. 2020). Much of the previous literature has focused on modelling the Galaxy and neutron star populations in a statistical sense (e.g. Sartore et al. 2010; Sharma et al. 2011), or if measured remnant positions are used, in terms of longitude, latitude or scale height distributions (van Paradijs & White 1995; White & van Paradijs 1996; Jonker & Nelemans 2004; Manchester et al. 2005; Olausen & Kaspi 2014; Repetto et al. 2017; Verberne & Vink 2021). However, there have been some attempts to measure correlations between neutron stars and Galactic structures in the plane of the Galaxy (e.g. clustering between OB associations and high-mass X-ray binaries, Bodaghee et al. 2012; Coleiro & Chaty 2013). Crucially, it is now possible to map spiral arms and star forming complexes throughout the Milky Way using masers (Reid et al. 2014, 2016, 2019). Doing this at other wavelengths, such as the optical (e.g. Russeil 2003; Gaia Collaboration et al. 2016) is difficult due to dust extinction, particularly further away from the Solar neighbourhood. There have also been studies looking at Milky Way global properties in the context

² frbhosts.org/

of Milky Way analogues (e.g. [Licquia et al. 2015](#)). With precise localisations and distance estimates, we can now see how neutron stars would appear distributed on the Milky Way, if viewed externally.

This paper is motivated by the magnetar-FRB connection, and as such there is a focus on magnetars and FRBs. However, studying how neutron stars in general relate to star formation in the Milky Way has a wider ranging relevance, for many classes of core-collapse and merger transients. There may also be implications for the evolutionary history of the Galactic populations themselves, and this will be the focus of a follow-up study, hereafter referred to as paper II ([Chrimes et al., in prep](#)).

This paper is structured as follows. In Section 2 the locations of Galactic magnetars, pulsars and X-ray binaries are mapped. Section 3 describes how the basic components of the Milky Way are assembled in order to produce a face-on ‘image’ of the Galaxy. The projected physical offsets between neutron stars, supernova remnants (SNRs), HII regions and spiral arms are discussed in Section 4, followed by the projected and host normalised offsets on the face-on disc of the Milky Way in Section 5. The enclosed fraction of flux within neutron star Galactocentric radii is investigated in Section 6, followed by fraction of light measurements in Section 7. The arm offsets, host offsets, enclosed fluxes and fraction of light distributions are all compared to samples of extragalactic transients. Section 8 presents a discussion of the uncertainties and implications, followed by concluding remarks in Section 9.

2 MAPPING NEUTRON STARS IN THE MILKY WAY

Neutron stars can be identified observationally in several ways. Here, we split the known Galactic population into magnetars (including SGRs and AXPs), pulsars (including binaries and millisecond pulsars), and X-ray binaries.

2.1 Magnetars

We use the McGill magnetar catalogue of [Olausen & Kaspi \(2014\)](#). The distances for each source are the most recent values in the literature, and the reasoning for each distance is listed in Table 7 of [Olausen & Kaspi \(2014\)](#). These include estimating the distance to an associated SNR, using the tip of the red giant branch in associated clusters, and X-ray inferred column densities. Distance uncertainties, where available, are taken from the primary distance reference in the catalogue. The distance for SGR 1935 is highly uncertain, with estimates from dispersion measures, dust extinction, a potentially associated SNR, and nearby molecular clouds (see [Bailes et al. 2021](#), for an overview). We adopt the [Bailes et al. \(2021\)](#) best distance estimate of 6.5 kpc, with a lower limit from their dispersion measure/dust analysis of 1.2 kpc, and an upper limit of 9.5 kpc the value assumed by [Bochenek et al. \(2020b\)](#).

Although the lack of a strong local bias in the magnetar sample suggests that selection effects are not significant ([Olausen & Kaspi 2014](#)), there is a dearth of magnetars on the far side of the Galactic centre (GC, at 8.2 kpc, [Gravity Collaboration et al. 2019](#)). This is despite the fact that γ -ray observatories have sufficient sensitivity to detect giant magnetar flares at extragalactic distances ([Burns et al. 2021](#)). Furthermore, we would not expect dust and neutral hydrogen gas to significantly attenuate such high energy photons. A similar effect has been noted before in the X-ray binary population ([Jonker & Nelemans 2004](#)), although in that case, detections are in softer X-rays and are more liable to HI absorption and source confusion

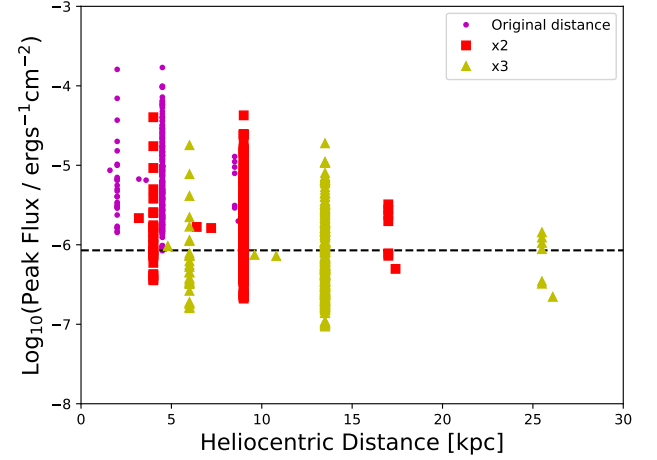


Figure 1. The peak burst fluxes of the 8 magnetars in the 5 year *Fermi* catalogue. Distance information is from ([Olausen & Kaspi 2014](#)). The sources are placed two and three times more distance and their fluxes are scaled accordingly. The minimum flux reported in the catalogue is indicated by the horizontal dashed line. Placing the sources beyond ~ 10 kpc often results in their bursts being below the faintest detected over 5 years. This implies that the Galactic magnetar sample is incomplete, rather than a significant fraction of the distances being underestimated.

effects that preferentially occur along sight-lines towards the Galactic centre.

There are three possibilities: that many of the magnetars have mis-assigned distances, that the sample really is incomplete, or that the effect is real and there fewer magnetars on the far side of the Galaxy (we deem this unlikely, given that spiral galaxies tend not to have large scale asymmetries of this nature). [Beniamini et al. \(2019\)](#) discuss the Milky Way magnetar sample, explaining that calculating completeness is non trivial when SGRs are detected in different modes (quiescence versus flaring) with different observatories.

To simplify the problem, we take the 8 magnetars from the 5 year *Fermi*/GBM magnetar burst catalogue ([Collazzi et al. 2015](#)). Distance estimates are provided in the McGill catalogue for each of these sources (SGR 0501+4516, 1E 1841–045, SGR J0418+5729, SGR 1806–20, SGR J1822.3–1606, AXP 4U0142+61, 1E 2259+586 and SGR J1550–5418). Some are detected multiple times over the 5 years, others just once. The peak flux of the detections is plotted versus distance in Fig. 1, with the flux reduced by factors of 4 and 9 to represent placing the sources two and three times further away. A horizontal line marks the faintest burst detected over the five years. For *Fermi* at least, many of these flares are not bright enough to be seen at >10 kpc. Using the original distance estimates, all 8 lie within 10 kpc and are by definition detected. At twice the distance, only 6/8 are within 10 kpc and 1 source would likely have not been detected. Three times further, and 4/8 lie beyond 10 kpc, while 3 magnetars would have been fainter than the faintest bursts in the 5 year catalogue. This demonstrates that burst luminosity and detector sensitivity are important factors in producing the dearth of known magnetars at large distances. [Beniamini et al. \(2019\)](#) conclude that the missing fraction in current catalogues is at least 0.3, possibly much more, a result which appears consistent with the trend shown here.

2.2 Pulsars

For pulsars, we use the ATNF catalogue (version 1.64, [Manchester et al. 2005, 2016](#)). Pulsars are far more numerous and have substantially weaker magnetic fields than magnetars, typically in the range 10^{11} - 10^{13} G. They have older characteristic ages and might, therefore, be expected to lie further from their birth sites, assuming similar natal kick velocities. The catalogue provides best estimate distances, inferred from parallaxes, HI absorption, globular cluster associations, nebular lines and stellar companions. Otherwise, the dispersion measure is used to infer a distance, in this case using the [Yao et al. \(2017\)](#) electron density model. Incompleteness is an even greater issue with this sample than for the magnetars, as shown in [Fig. 2](#). However, the pulsars are sufficiently numerous that a cut can be placed at high luminosity, such that the entire Galaxy is covered in a less biased way, with the exception of the known dearth of pulsars in the Galactic centre. This is due to lower survey sensitivity limits along central sight-lines ([Rajwade et al. 2017](#), we will later demonstrate the effect this has on the pulsar fraction of light distribution). The chosen cut is 65 mJy kpc^2 . This is the lowest cut that yields numbers on either side of the GC heliocentric distance that are consistent within Poisson uncertainties. To make the numbers exactly equal requires a harsh cut, reducing the total to only a handful of sources. Our chosen cutoff is a compromise between sample size and completeness, but we later vary this threshold to determine the impact. Within this sample, we also define a subset of young pulsars ($< 10^5$ yrs), which should in principle comprise a similar population to magnetars.

2.3 INTEGRAL low-mass X-ray binaries

XRBS are systems containing an accreting black hole or neutron star; low mass XRBS (LMXBs) have a donor star masses that are typically $\lesssim 2.5 M_{\odot}$. Although still subject to luminosity-distance completeness issues, XRBS benefit from having a maximum theoretical luminosity (the Eddington luminosity) and therefore distances can be approximated from the X-ray observations alone, in the absence of other indicators ([Jonker & Nelemans 2004](#)). We use the INTEGRAL ([Winkler et al. 2003](#)) sample of [Sazonov et al. \(2020\)](#). This sample consists of LMXBs detected by the hard X-ray sensitive telescope IBIS.

[Krivonos et al. \(2017\)](#) show the distance contours at which X-ray sources of given luminosities can be detected in the INTEGRAL survey. The majority of the Galaxy is covered with high completeness down to hard X-ray luminosities of $2 \times 10^{35} \text{ ergs}^{-1}$, which is the lower end of the LMXB luminosity distribution. The sensitivity map provided by [Krivonos et al. \(2017\)](#) shows that coverage is not uniform, as total survey time varies with Galactic longitude. However, the sensitivity contours can be approximated as circular from a location that is $\sim 3 - 5 \text{ kpc}$ closer to the Galactic centre than the Sun (see figure 2 of [Krivonos et al. 2017](#)). Since the $2 \times 10^{35} \text{ ergs}^{-1}$ limit is $\sim 20 \text{ kpc}$ away from this point in all directions, only the outskirts of the Galaxy are affected by survey biases, which should be of minimal impact. As the accretor type (i.e. neutron star or black hole) is often ambiguous, we do not attempt to separate them. The XRB populations in this paper therefore include a small contribution from black hole systems.

2.4 INTEGRAL high-mass X-ray binaries

A review and catalogue of INTEGRAL-detected high-mass X-ray binaries (HMXBs) is presented by [Kretschmar et al. \(2019\)](#). HMXBs are typically neutron stars (although black hole systems also exist),

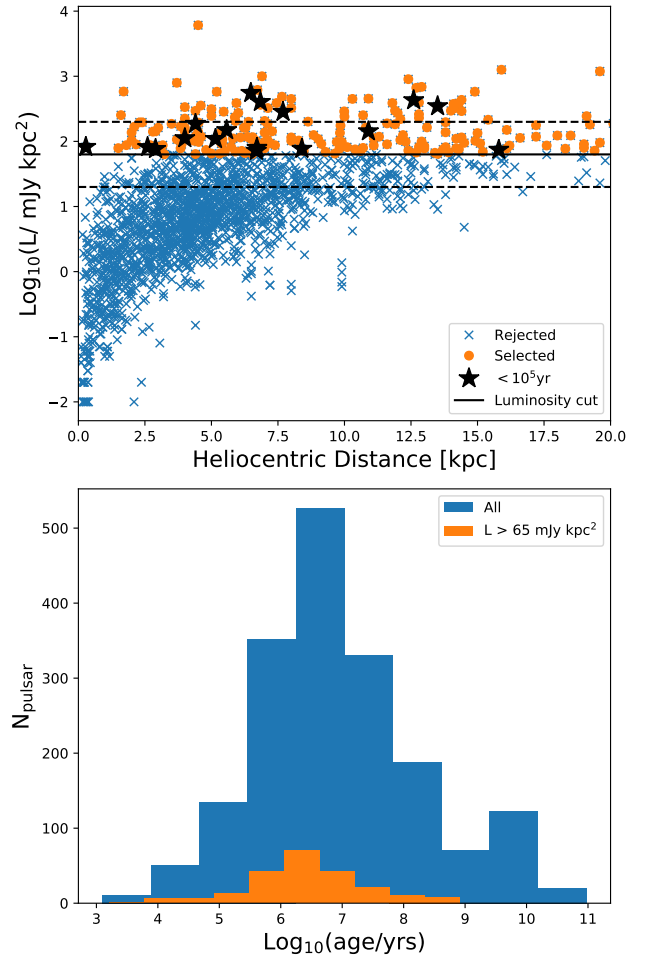


Figure 2. Upper panel: ATNF catalogue pulsar 1.4 GHz luminosities versus the best distance estimates. A cut is applied at 65 mJy kpc^2 , which removes much of the strong local disc bias in the sample and gives (approximately, with the exception of the Galactic centre) equal coverage across the Galaxy. Two alternative cuts (± 0.5 dex) are shown by dashed lines, these are later used to demonstrate the impact of different choices. Stars indicate the pulsars with ages similar to magnetars. Lower panel: spin down ages, defined as $\tau = P/2\dot{P}$. Selecting the most luminous pulsars slightly shifts the sample towards younger sources. In $\log_{10}(\text{age}/\text{yrs})$, the full sample has a median and standard deviation of 6.8 ± 1.4 , compared to 6.5 ± 0.9 for the bright pulsars.

accreting material from a $\gtrsim 5 M_{\odot}$ companion. They are among the brightest X-ray sources in the Galaxy. As HMXBs contain massive stars, they are observed to correlate in Galactic longitude with tangents to the spiral arms and star forming complexes ([Bodaghee et al. 2007](#); [Coleiro et al. 2013](#); [Coleiro & Chaty 2013](#)). Where available, some distances in the catalogue of [Kretschmar et al. \(2019\)](#) were estimated from *Gaia DR2* parallaxes of the optical counterpart, which has introduced a local bias in the sample with measured distances. The projected locations therefore reflect both their actual locations and survey/catalogue biases. When a distance is uncertain and a range is given, we use the mean of the upper and lower estimates. We later quantify the effect of the local bias on our F_{light} results, by restricting the analysis to the disc. As for the LMXBs, we do not separate black hole and neutron star systems.

3 BUILDING A FACE-ON MILKY WAY IMAGE

3.1 Spiral arms

In order to map out where ongoing star formation is occurring in the Milky Way, we follow the approach of Reid et al. (2019), who use water and methanol masers to trace out the spiral arm structure in 3D. Masers are uniquely suited to this, as they are numerous, bright, and their detection is relatively unaffected by foreground absorption. In brief, Reid et al. (2016) and Reid et al. (2019) use parallax measurements of various maser sources (star forming complexes, young stellar objects, AGB stars and others, Valdetaro et al. 2001; Pestalozzi et al. 2005; Green et al. 2017; Anderson et al. 2012b; Urquhart et al. 2014) to infer the spiral arm positions and parameters locally, including pitch angle and tightness. The arms are then extrapolated around the entire Galaxy. Because radio observations of masers yield radial velocities, which can be converted into a local standard of rest velocity V_{LSR} , the velocity structure of the Galaxy can be mapped out to distances beyond where parallaxes can be measured. They develop a Bayesian code, with the estimated arm positions as a prior, that can infer the likeliest distance given only a Galactic latitude, longitude and LSR velocity.

Beyond 3 kpc, the completeness of the input catalogues drops off as a function of distance from the Solar System (inverse square law) and Galactocentric radius (mainly due to source confusion towards the Galactic centre). However, the sources that are detected at >3 kpc can still be used to trace the spiral arms, through the use of the Bayesian code. The code includes a prior (0 to 1) for whether the source is near or far, as the V_{LSR} measurements contain a distance degeneracy for sight-lines along a circular path. We follow the same methodology, setting the near/far prior to 0.5, but restrict ourselves to the Red MSX catalogue of Urquhart et al. (2014, see also Lumsden et al. (2013)). Although less Galactic structure is mapped out, the luminosity distribution of the sample is well understood, as is the incompleteness as a function of distance. We further limit the sample to HII regions and young stellar objects (YSOs), in order to trace out star formation. The resultant maser catalogue comprises 1644 sources. This catalogue is not complete in terms of luminosity, nor is this necessarily the aim. We want a Galactic map that is *uniform* in its incompleteness, so the shape of the Galaxy is accurately mapped out. This methodology should result in that outcome, provided that the luminosity function of masers is constant across the Galaxy. Limiting ourselves to a single, well understood catalogue also avoids double counting star forming complexes or single sources that appear in multiple maser catalogues.

Taking the HII regions and YSOs of Urquhart et al. (2014), we run the Bayesian distance FORTRAN code of Reid et al. (2019) and obtain a Milky Way map. To compensate for the high level of incompleteness at larger distances (>3 kpc) we again follow the method of Reid et al. (2019). Random points (sprinkles) are added at x , y and z offsets from each maser position, as a function of distance from Earth and Galactocentric radius. More random sprinkles are added at larger distances, and the width of the Gaussian used to determine the random offsets from the existing maser positions increases with Galactocentric radius (to reflect the widening spiral arm width). This process is described by the following. The number of sprinkles added per maser is given by,

$$N_{\text{sprinkle}} = \left(\frac{D}{3\text{kpc}} \right)^2 - N_{\text{corr}} \quad (1)$$

for distances greater than 3 kpc. The maximum number added is 10, and the minimum 1. N_{corr} is a correction to the form given by Reid et al. (2019), which is necessary given our smaller input catalogue

size. Sprinkles are added in order to match the density of sources in the complete local (~ 3 kpc) neighbourhood. The N_{sprinkle} sources are added according to Gaussians in x , y and z . The standard deviations are given by,

$$\begin{aligned} \sigma_z &= 20 + 36(R_g - 7.0), R_g > 7 \\ \sigma_z &= 20, R_g < 7 \end{aligned} \quad (2)$$

for the height (in pc) out of the Galactic plane, where R_g is the Galactocentric radius (in kpc). The scale height increases with Galactocentric radius, as observed, and the plane of the masers is also warped (see Reid et al. 2016, for details). We also have for the x and y coordinates,

$$\sigma_{xy} = \frac{336 + 36(R_g - 8.15)}{W_{\text{corr}}} \quad (3)$$

where W_{corr} is an arm width correction, again needed in order to tune the random sprinkling to match the local density of points. In Reid et al. (2019), with their large input catalogue, $N_{\text{corr}} = 0$ and $W_{\text{corr}} = 1$.

Before we tune these parameters to produce the map, a final issue is that there is a dearth of sources in a cone of around ~ 30 degrees toward the Galactic centre. On our side of the Galactic centre, this is corrected for by joining the arms and sprinkling points along these curves so that their number and density is comparable to the arms either side. For the opposite side, we simply mirror the ~ 30 degree slice of the Galaxy on our side. The result is that the arms do not smoothly join, and the maser positions here are arbitrary. However, it does ‘complete’ the Galaxy in terms of luminosity. This is required for some of the F_{light} calculations in Section 7.

3.2 Testing the spiral arm map

In order to tune the incompleteness corrections described by equations 1, 2 and 3, we consider two metrics that should be approximately constant as a function of Galactocentric azimuthal angle. The first is the mean distance to the nearest neighbouring point as a function of Galactocentric radius, and the second is the mean number of points within a fixed distance, again as a function of radius. These metrics are compared for (i) sources with 3 kpc, (ii) those in the heliocentric distance range 3 – 8 kpc, and (iii) those beyond 8 kpc. We find that the default $N_{\text{corr}} = 0$ and $W_{\text{corr}} = 1$ values from Reid et al. (2019) provide a poor agreement between local sources and the rest of the Galaxy, given our smaller input catalogue. Sampling integer values in the range 0-8, $N_{\text{corr}} = 6$ and $W_{\text{corr}} = 5$ provide the best match in terms of χ^2 between the local and more distant regions, the result is shown in Fig. 3.

The resultant maser map is shown in Fig. 4. To compare the arm positions to other Milky Way spiral arm maps, references include Vallée (2002), Russeil (2003), Vallée (2008) and Churchwell et al. (2009), in addition to electron density models (e.g. Cordes & Lazio 2002).

Counting masers on either side of the Galactic centre, and on the left and right hand sides, yields 2958, 2867, 3268 and 2557 sources respectively. There is therefore a larger disparity in the left/right hand halves than on our side versus the opposite side of Galactic centre, although there are still fewer points at $y > 8$ kpc as made clear by the mirrored section. This arises because (i) we are adding extra points based on the locations of the existing points and (ii) the arm widths are relatively narrow. As a result, longer spatial scales (the inter arm regions) are not filled in at large distances. However, this is likely to be a small effect as the majority of the maser luminosity is contributed by the spiral arms. Arm gaps are also less efficiently

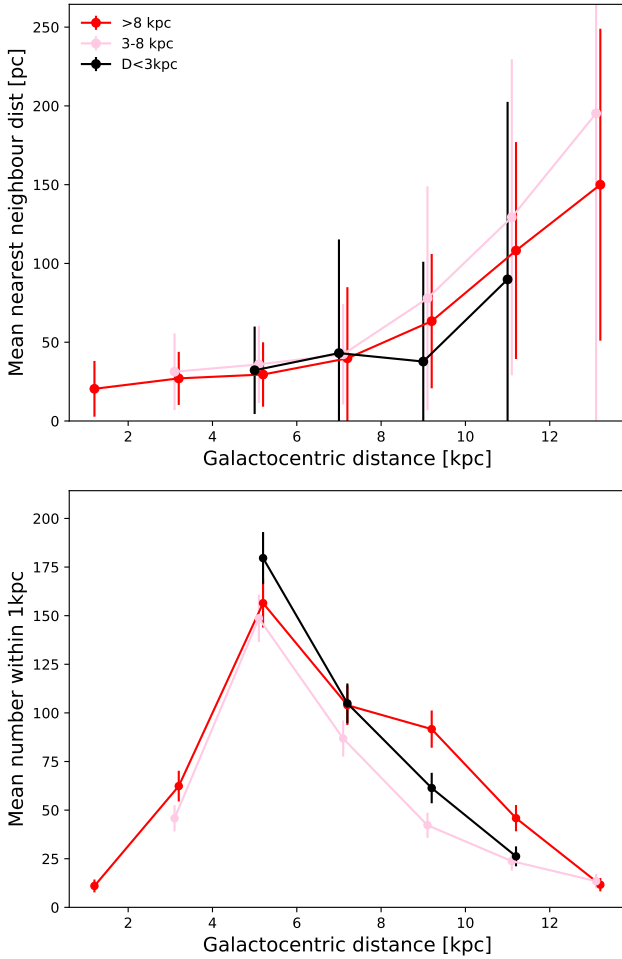


Figure 3. Upper panel: the mean distance to the nearest neighbouring maser, following the method of Reid et al. (2019) as described in the text. The 3 heliocentric distance ranges have approximately equal maser density as a function of Galactocentric distance. Lower panel: The mean number of masers within 1 kpc of each maser, again as a function of radial distance from Galactic centre. The arm width and N_{sprinkle} functions used to add artificial masers are given in equations 1, 2 and 3.

filled in at large distances, but we will later investigate the impact of this residual spatial incompleteness on our results.

The sources are also assigned a bolometric luminosity. Inside 3 kpc, the catalogue is complete down to $1000L_{\odot}$. For the real masers, we simply assign the value reported by Urquhart et al. (2014). Outside 3 kpc, the randomly sprinkled points are assigned a luminosity drawn randomly from the distribution below the completeness limit at that distance. In this way, the luminosity function should be the same across the map, complete down to $1000L_{\odot}$ everywhere. Again comparing our side, the opposite side, left and right, summing the maser luminosities in these halves yields $\text{Log}_{10}(L_{\text{bolo}}/L_{\odot})$ values of 7.82, 7.61, 7.75 and 7.70. In Fig. 4, the opacity and size of the maser points is proportional to $\text{Log}_{10}(L_{\text{bolo}}/L_{\odot})$.

3.3 Placing Galactic neutron stars on the map

The magnetar positions on the maser map are shown in the left panel of Fig. 4. Their positions have been computed from the Galactic lat-

itude, longitude, and given distance, correcting for a Solar System height above the Galactic plane of 15 pc (Olausen & Kaspi 2014, although this negligible for our purposes). They are coloured according to their height above or below the plane. We do not consider the magnetars in the Magellanic clouds (one is known in each), again due to the distance-completeness issue.

Throughout this paper, we adopt a y -coordinate cut of < 8.3 kpc, for both image pixels and the neutron stars themselves, unless stated otherwise. There are a few key reasons for this:

- The neutron star samples have biases against detection at large distances (see Figs. 1 and 2),
- Distance uncertainties tend to be larger further away (see e.g. the magnetars on Fig. 4, or the region within which *Gaia* parallax distances can be estimated), and,
- The mirrored section of the maser map does not represent real arm locations and including this area would produce inaccurate radial flux profiles and F_{light} distributions.

This cut approximately halves the galaxy at Galactic centre, but ensures that the centrally located magnetar SGR 1745–2900 is not excluded from any distributions. This would be unrepresentative given that we know of at least one magnetar in the central ~ 100 pc of the Galaxy. We expect that Galactic populations on our side, versus the other side, of Galactic centre should be similar. Therefore comparisons between Galactic samples at $y < 8.3$ kpc and extragalactic samples that cover the whole range of Galaxy locations should be fair, to first order. The other neutron star samples have been placed on the 2D map in Fig. 4 in the same way. The selected bright pulsars, INTEGRAL LMXBs and HMXBs are shown in the right hand panel as black circles, blue squares and orange triangles, respectively.

There are **two exceptions** to our $y < 8.3$ kpc cut - (i) when considering F_{light} uncertainties (as the distance errorbars can extend beyond 8.3 kpc) and (ii) when creating sub-regions B and C within the Galaxy, to investigate the effects of incompleteness and low number statistics. We will return to this in detail in Section 7. Until then, all analyses are restricted to < 8.3 kpc, both in terms of the objects themselves and the image pixels.

3.4 The disc, bulge and bar

In addition to the arms, the Milky Way has a disc (in which the arms are embedded) and a central bulge/bar. Our basic model follows Widrow et al. (2008), with additions and edits based on subsequent mapping efforts. We model the disc with an exponential profile, making no distinction between the thin and thick disc, and adopting a scale length of $R_d = 4$ kpc. This value is based on the range found by Kumar et al. (2020), and is at the upper end of most previous literature estimates (e.g., Boissier & Prantzos 1999; Siegel et al. 2002; McMillan 2011; Chen et al. 2017). However, it is more consistent with Milky Way analogues, potentially resolving an issue noted by Boardman et al. (2020), where the Milky Way’s disc was unusually compact. The bulge is modelled as a Sérsic profile with index $n = 1.32$ and half-light radius $R_d = 0.64$ kpc. To account for the bar, this is convolved with the bar profile as mapped by Mira variables in *Gaia* (Grady et al. 2020). The angle between the Sun-Galactic centre line and bar semi-major axis is 20° (e.g. Binney et al. 1997; Grady et al. 2020).

3.5 Weighting the components

The three components - a smooth disc, embedded arms and bulge/bar - now need weighting to represent their respective contributions to

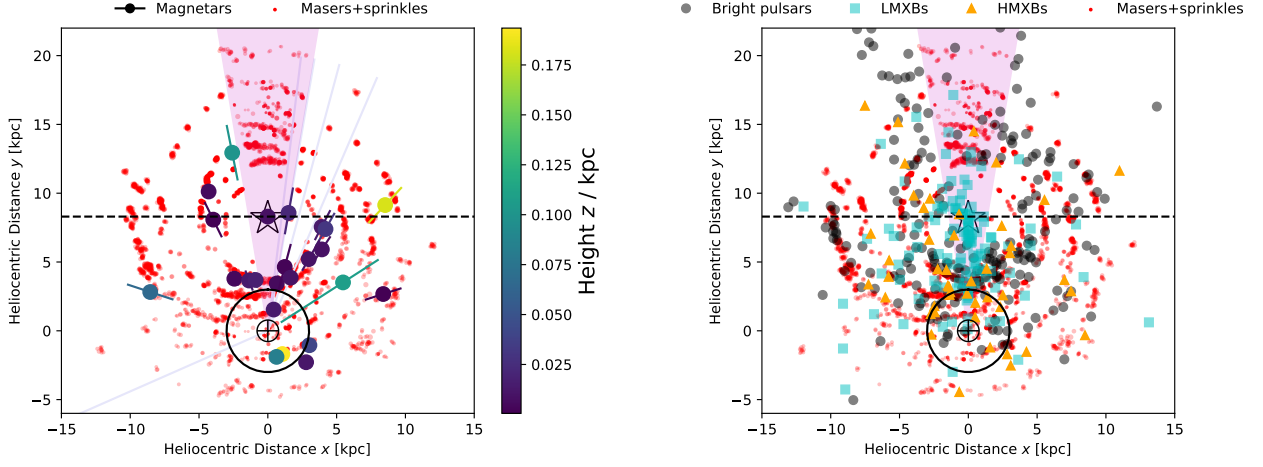


Figure 4. The Milky Way maser map produced with the methodology of Reid et al. (2019), overlaid with magnetars positions (left, coloured by height above the plane, Olausen & Kaspi 2014) and pulsars/LMXBs/HMXBs (right, black circles, blue squares and orange triangles, Manchester et al. 2005; Sazonov et al. 2020; Kretschmar et al. 2019). For magnetars with unknown distances, grey lines are drawn in their direction. We are located at (0,0), and a 3 kpc radius circle is indicated - this is the region which we are trying to match throughout the Galaxy in terms of maser density. The region where maser detections are limited is shaded (in an opening angle of 30 degrees towards Galactic centre, marked with a star). On this side we fill in the small arm gaps as described in the text. The opposite side of Galactic centre is filled in by mirroring our side of the Galaxy. This demonstrates how well incompleteness has been corrected for at the largest distances, but this area is not used in analyses, unless stated otherwise. The region below the dashed horizontal line is used for the majority of measurements going forward, to limit the impact of heliocentric distance uncertainties and detection biases.

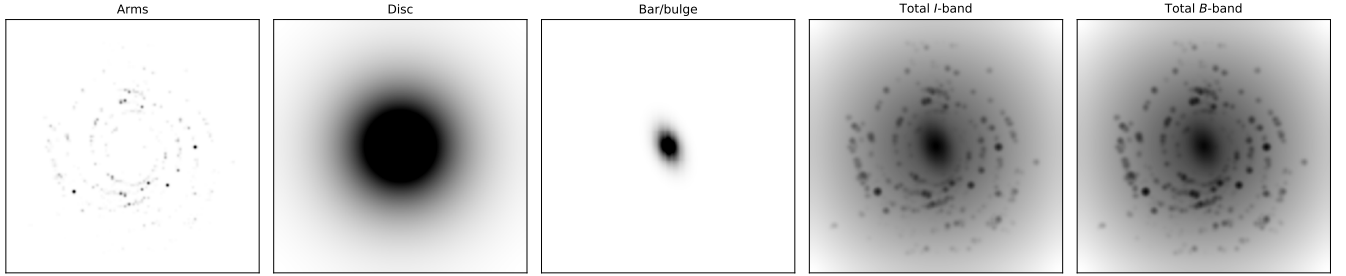


Figure 5. The three Galaxy components used, and their combination (with appropriate scaling) to produce the *I* and *B*-band images.

the total luminosity of the Milky Way. This will also be wavelength dependent.

As a starting point, we take the bulge and disc luminosities of Flynn et al. (2006), where the disc includes the arms. The *I*-band bulge and disc luminosities are $10^{10}L_{\odot}$ and $3 \times 10^{10}L_{\odot}$ respectively. These numbers are consistent with the later results of Bland-Hawthorn & Gerhard (2016), who carry out a kinematic study, determining that the stellar mass of the Galaxy is $5 \pm 1 \times 10^{10}M_{\odot}$. They estimate an *I*-band mass to light ratio of 1.18, based on SDSS galaxy analogues, giving a total *I*-band luminosity of $4.2 \times 10^{10}L_{\odot}$. They further estimate that the mass of the bulge and central embedded disc is $1.5 \times 10^{10}M_{\odot}$, in good agreement with our adopted values.

The procedure described in Section 3.1 means that we have a value for the total bolometric luminosity of the masers above the $1000L_{\odot}$ limit, $10^{8.25}L_{\odot}$. This is twice the Urquhart et al. (2014) estimate for the total contribution of high mass embedded star formation to the Galactic luminosity (due to differences in incompleteness corrections). However, for our purposes we are only interested in the spiral arm locations, and the *relative* flux contributions of the galaxy components.

We adopt an arm strength of 0.15 in the *I*-band, typical for Milky Way mass galaxies (e.g. Díaz-García et al. 2019; Yu & Ho 2020).

This is defined as the ratio of disc surface density arising from the $m = 2$ spatial Fourier component, versus the $m = 0$ component (Seigar & James 1998). It therefore quantifies the proportion of disc light arising from short spatial scales (i.e., the spiral arm structure). Arm strength varies in different bands, as the spiral arms are usually slightly bluer than the disc - for *I*-band strengths of 0.15, typical *B*-band strengths are ~ 0.2 , values which we use going forward (Yu et al. 2018).

Working with our initial $10^{10}L_{\odot}$ and $3 \times 10^{10}L_{\odot}$ bulge/disc *I*-band values, and using the masers as a proxy for the arm luminosity, the disc must have a luminosity of $10^{8.85}L_{\odot}$. The bulge/bar is one third of this, so $10^{8.37}L_{\odot}$. The constants in the exponential disc and Sérsic profiles are scaled to reflect these respective contributions to the *I*-band light.

The *I*-band, however is a better tracer of stellar mass than star formation. To obtain a bluer version of the image, we use the *B*-*I* colours of Licquia et al. (2015), who estimate a total integrated Galaxy colour of 1.77. Bland-Hawthorn & Gerhard (2016) obtain a value of 1.85 for the whole Galaxy, but with 0.1 mag uncertainties, so this is consistent with Licquia et al. (2015). Note that all BVI colours quoted in this paper are in the Vega system, but they are converted to AB magnitudes to perform any calculations. We now need either

the colour of the disc or bulge in order to determine the B -band luminosities of all three components. Flynn et al. (2006) provide a local disc $B-I$ colour of 1.48, but this has been corrected for dust and is therefore artificially blue. We instead follow the rationale of Licquia et al. (2015). They base their Galaxy colours on extragalactic analogues chosen for their mass and SFR similarity to the Milky Way. Within these analogues they identify a bulge-dominated subsample, which has a mean B -band mass-to-light ratio (MLR) of 4.1. We also use their global MLR estimates in I and B of 1.29 and 1.89, and a bulge-to-total mass ratio of 0.3 (Bland-Hawthorn & Gerhard 2016). Taking the I -band component luminosities from Flynn et al. (2006), this implies a bulge/bar $B-I$ of 2.41. This compares well with Galactic bulge observations through the relatively dust-free Baade’s window (Rich et al. 2020; Lim et al. 2021). The inferred disc colour is 1.62, bluer than the total integrated colour as expected, and 0.14 redder than the dust-corrected Flynn et al. (2006) value for the local disc. The colour difference between the bulge and disc is large compared to other spiral galaxies (Cameron et al. 2009), but the values are otherwise in good agreement with the observational constraints listed. Given a total $B-I$ of 1.77, a disc colour of 1.62 and a bulge colour of 2.41, the B -band bulge/bar is ~ 5.6 times fainter (~ 2 magnitudes) and the disc/arms only ~ 2.7 times fainter (~ 1 magnitude) than in the I -band.

3.6 The final Milky Way image

The construction of the final Galaxy image is shown in Fig. 5, in both bands. These images have a pixel scale of 250 pc/pix, and we have applied a Gaussian blur with a FWHM of 2 pixels to simulate *Hubble Space Telescope*, (*HST*) quality imaging (~ 0.05 arcsec pix $^{-1}$). The masers are treated as point sources, and their luminosity is assigned to whichever pixel they fall under. In reality they are not point sources, but this unlikely to be a significant issue, as the majority of star forming regions have radii < 250 pc, and almost all < 500 pc (Wisnioski et al. 2012). This effect is further diminished as they tend to have approximately Gaussian density profiles, so that the light contributed to neighbouring pixels will not usually be a significant fraction of the total star forming region luminosity.

Although it has been known for decades that spiral arms represent overdensities where star formation is enhanced (Roberts 1969; Schweizer 1976), it is worth considering whether our B -band image in particular really reflects where star formation occurs. A good test of this is to look at nearby extragalactic sources in terms of both masers and other star formation tracers such as UV light. Barred spirals without AGN are the best analogues of the Milky Way (see e.g. Fraser-McKelvie et al. 2019; Boardman et al. 2020). Colina et al. (1997) provide spatially resolved *Hubble Space Telescope* (*HST*) WFC2/F128W observations of NGC 3351 (M95), which fits these criteria. The UV structure of this galaxy is strikingly similar to the Milky Way maser map produced using the method of Reid et al. (2019): the spiral arms, bar, and a nuclear ring are prominent. It has also been shown that (in the absence of AGN) stronger star formation produces stronger masers (see e.g. the SWAN survey, Gorski et al. 2018). Another good reference point is the PHANGS-*HST* survey of local (< 20 Mpc) star-forming galaxies (Lee et al. 2021). Here, the same trend of young stellar associations following spirals arms, and nuclear ring structures, is also seen. It is therefore reasonable that the maser map we have produced with the methodology of Reid et al. (2019) and catalogue of Urquhart et al. (2014) genuinely reflects where the bulk of ongoing star formation is occurring in the Milky Way.

4 STAR FORMING REGION OFFSETS

Having constructed our neutron star samples in Section 2, and a Milky Way model in the Section 3, we now move on to measuring how neutron stars are distributed with respect to Galactic structures and light. We start with their offsets from star forming regions.

Measurements of the projected physical offset from the nearest star forming region have been possible for a few FRBs so far: FRB 121102 (Bassa et al. 2017, < 0.7 kpc, encompassed by the star forming region), FRB 180916B (Tendulkar et al. 2021, ~ 250 pc from the centre of the nearby star forming region) and FRB 190608 (less than ~ 500 pc from a bright knot of star formation in the host at 1σ uncertainty, Chittidi et al. 2020). We now measure the physical offset of the magnetars, pulsars and XRBs from their nearest maser, a good proxy for the nearest spiral arm. These offsets are in 3D, but the typically low Galactic latitudes mean that the face-on, 2D offsets are similar. The warp of the disc is accounted for in the maser positions (see Reid et al. 2016). The resultant cumulative distributions are shown in Fig. 6. It is important to note that we are not necessarily claiming that the nearest star forming region/spiral arm is the birth site of the system. Instead, this is a simple measurement which we can compare to the offsets of transients (in particular FRBs) within their hosts.

The impact of heliocentric distance uncertainties on the magnetar distribution is estimated by varying the distance within the upper and lower values listed in the McGill catalogue (and distance references therein). Where an uncertainty has not been estimated, a 15 per cent error on the distance is assumed, the mean of the uncertainties that are available. The maximum and minimum maser offset within this heliocentric distance range produces the shaded band in Fig. 6. The magnetars are less offset from star forming regions than pulsars or XRBs, but there is significant overlap within their uncertainties. The two extragalactic FRB offsets are highlighted, as is the putative Galactic FRB source. To see if the extragalactic FRB offsets are consistent with the Galactic populations, we perform bootstrapping with resampling and 10000 samples. The probability of selecting three sources at $D < 700$ pc from the magnetar sample is 0.51, 0.64 for HMXBs, 0.65 for young pulsars, 0.47 for the whole bright pulsar sample and 0.07 for LMXBs. Statistically this does not rule out any sample, but disfavors the older LMXBs and demonstrates that the FRB offsets observed so far are not inconsistent with a young neutron star origin.

We briefly compare our offset results to other studies. The HMXB results are in good agreement with the findings of Bodaghee et al. (2012) and Coleiro & Chaty (2013), who find that they are correlated with OB associations and star forming regions on scales of ~ 300 -400 pc. The D_{nearest} distributions are also similar to the XRB results of Arnason et al. (2021), who use *Gaia* DR2 heliocentric distances to infer XRB-spiral arm offsets (using the spiral arm model of Vallée 2008). They find a median XRB-arm offset of ~ 600 pc, compared to our HMXB value of ~ 400 pc - ours is *lower*, counter to the expected effect of maser incompleteness, although the wider distribution of masers (i.e., there are some in inter-arm regions) may be responsible. Our range of nearest maser distances is also comparable to their range of nearest arm distances, with both spanning a few tens of pc to a few kpc. We note that Arnason et al. (2021) find a smaller difference between HMXBs and LMXBs. Looking the spatial distributions in Fig. 4, this likely because the use of *Gaia* distances biases the study to the disc, whereas our results include proportionally more LMXBs in the bulge, where there is lower ongoing star formation and hence a dearth of masers. Overall however, given the similarity between our nearest-maser results, and those which use analytic arm models

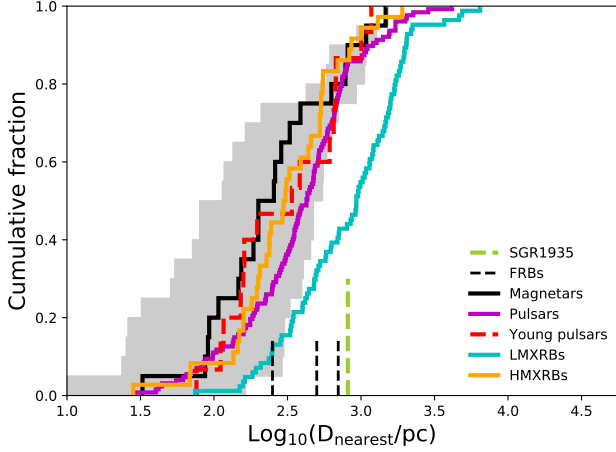


Figure 6. The distance of each magnetar, pulsar and XRB to the nearest maser, a good approximation for the offset from the nearest spiral arm. The grey shading indicates the minimum and maximum maser offsets for each magnetar, when their heliocentric distances are varied within the given uncertainties (Olausen & Kaspi 2014, and Table A1 of the appendix). The three FRB offsets from bright star forming complexes within their hosts (or upper limits on the offset) are consistent with neutron star-star forming region offsets in the Milky Way, including magnetars.

and *Gaia* DR2 distances, we conclude that our results are indeed representative.

We provide Anderson-Darling (AD) test results between the samples in Table 1. Results which fail result to reject the null hypothesis that any two distributions are drawn from the same underlying population are in bold font (> 0.05 , or $\sim 2\sigma$ significance). Results which do not round up to 0.01 are simply listed as 0.00. The maximum value is 0.25, as outputs are capped at this value by the `scipy` Anderson function. The assumed magnetar distances are used (i.e. the solid black line in Fig. 6). Although the upper end of the uncertainties overlap with the HMXBs and pulsars, we expect the magnetars to be *less* offset than estimated here rather than more. This is because heliocentric distance uncertainties should preferentially scatter them away from their natal star forming regions, assuming they were born in star forming regions, and given that inter-arm regions take up more volume than the arms. The progression in offsets is apparent in the AD-test results, where aside from the LMXBs, the samples tend to be more consistent with the neighbouring samples in the progression. The LMXB difference is due to their concentration in the Galactic bulge, a region with a dearth of masers.

We might assume that magnetars have the smallest star forming region offsets because they are the youngest, and have had less time to travel from their birth site at their natal kick velocity. There is a clear progression from the least offset magnetars (ages $\sim 10^3$ - 10^5 yrs), to the (old) pulsars and LMXBs, whose age distributions extend up $\sim 10^{10}$ yrs. These older systems have likely lost any correlation with their original birth site. For the younger neutron stars, since we have age ($P/2\dot{P}$) and distance information, a minimum kick velocity can be approximated as the distance to the nearest spiral arm (maser) divided by the spin-down age estimate. However, due to the very young age estimates ($\sim 10^3$ - 10^5 yr) of magnetars (Olausen & Kaspi 2014) this results in unrealistic velocities of up to 10^5 - 10^6 km s $^{-1}$, orders of magnitude above Galactic neutron star (including magnetar) velocities inferred from proper motions (Hobbs et al. 2005; Tendulkar et al. 2013). Indeed, this argument has been used to rule out a magnetar origin for FRB 180916B, which is ~ 250 pc away from a star forming

Table 1. AD-test results for comparisons between the Galactic sample nearest maser offsets. Results that show statistical consistency (> 0.05 p-value) are shown in bold with grey shading. The progression of offsets from magnetars to LMXBs in Fig. 6 is also reflected in the significance of the differences between the distributions. With the exception of LMXBs which are distinct, the samples are more consistent with neighbouring samples in the progression. As throughout unless otherwise stated, we only consider objects at $y < 8.3$ kpc (see Fig. 4).

	LMXBs	Pulsars	Y. Pulsars	HMXBs
Magnetars	0.00	0.06	0.25	0.25
HMXBs	0.00	0.20	0.25	-
Y. Pulsars	0.00	0.25	-	-
Pulsars	0.00	-	-	-

region in its host (Tendulkar et al. 2021). However, the interpretation of these velocities as kicks breaks down, because around half of the Galactic magnetars have a claimed SNR association (Olausen & Kaspi 2014). Assuming a core-collapse origin, this implies that the distance from the arms was travelled primarily by the *progenitor*.

We will explore the implications of this for magnetar progenitor channels, natal kicks and progenitor velocities, in paper II. In the context of viewing Milky Way neutron star locations from afar, the key point is that offsets of ~ 100 s of parsec (as seen in FRB 180916B) are not inconsistent with a magnetar origin.

5 PROJECTED GALAXY OFFSETS

We now look at the offsets of the neutron stars from the Galactic centre, and compare to extragalactic transient offsets from their host barycentres. We also use the radial Galactic SNR distribution of Verberne & Vink (2021), derived from their longitudinal positions, as SNRs should in principle trace the locations of young neutron stars. Both offsets δr and host-normalised offsets $\delta r/r_e$ are shown in Fig. 7, where r_e is the half-light radius. For our Milky Way image, $r_e = 3.75$ kpc in the *B*-band and 3.28 kpc in the *I*-band. The results of AD-tests between the magnetars/pulsars/young pulsars/XRBs/SNRs and the comparison samples are listed in Table 2. Across the six Galactic samples, FRBs most frequently have a p-value > 0.05 . Only the *I*-band normalised results are shown in Fig. 7, using the *B*-band half-light radius results in slightly less offset distributions (these values are available for the magnetars in Table A1 of appendix A). After FRBs, Ca-rich supernovae perhaps stand out as being the second best match in terms of physical offsets. However, raw offsets are less informative as they depends on the host size, and therefore we would need to compare against Milky Way-like galaxies for a fairer comparison.

The measured Galactocentric offsets depend on the heliocentric distances assumed. The magnetar distances are derived from a diverse set of methods, and the uncertainties are often poorly quantified (see Table A1 of the appendix for details). As an extreme limit, we take the the maximum and minimum offsets possible along the line of sight, assuming that the magnetar lies ‘inside’ the Galaxy (i.e. < 12 kpc from Galactic centre). The region bounded by the minimum and maximum possible distributions is shaded light grey in Fig. 7. We also take the listed uncertainties, and use the quoted upper and lower bounds. Where an uncertainty is not given, we assume an uncertainty of ± 15 per cent of the distance (the mean uncertainty of those where an estimate has been made). Shading between the upper and lower distributions produces the narrower dark grey band. Even if we consider the lowest offsets that the magnetars could possibly

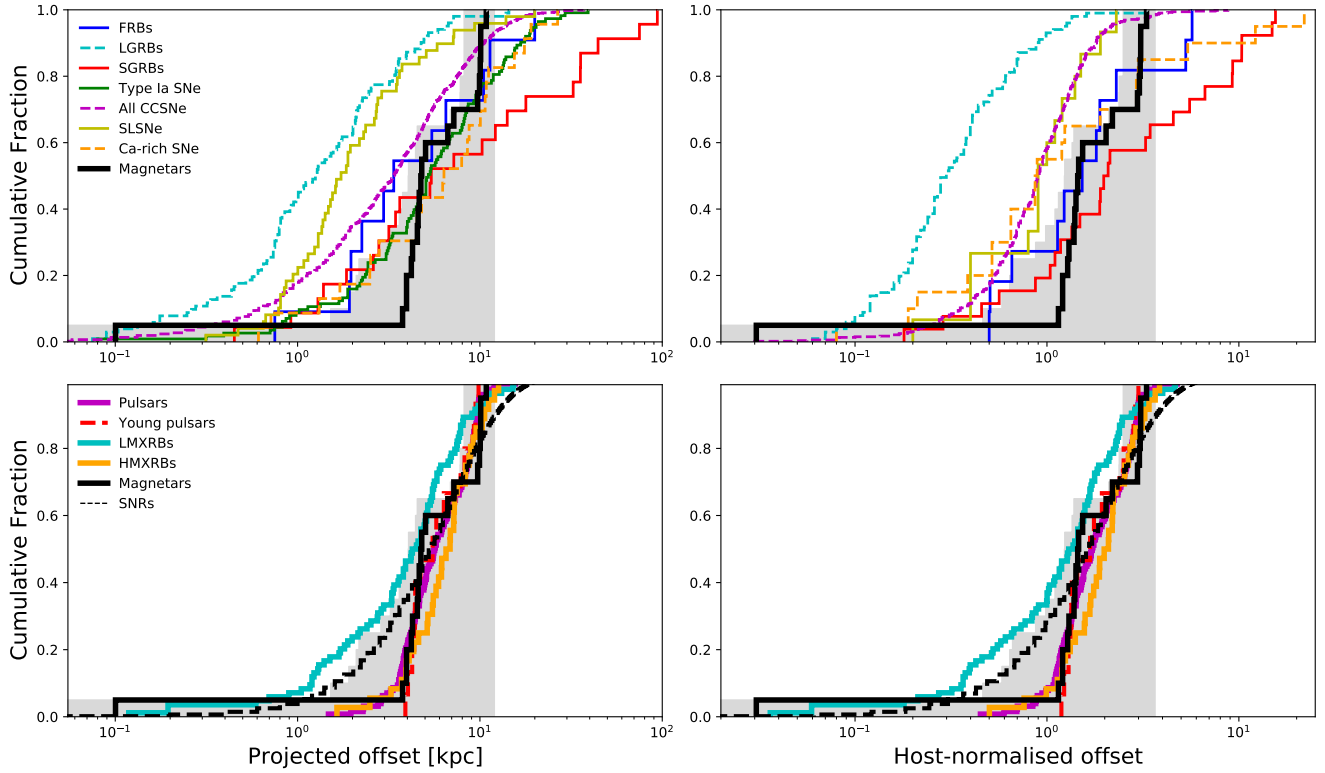


Figure 7. Projected (left) and host normalised (right) offsets for Milky Way magnetars, compared to the offsets of extragalactic transients on their hosts (top row) and other Galactic neutron star systems (bottom row, shown separately for clarity). We also show the exponential SNR distribution of Verberne & Vink (2021). FRB 20200120E has been added to the FRB offset dataset, assuming association with M81 (Bhardwaj et al. 2021). The light grey shaded region is bounded by the extreme upper and lower distributions for the magnetars, assuming the maximum and minimum offsets possible along that line of sight (and that the magnetar lies ‘in’ the Galaxy, at $\delta r < 12$ kpc). The narrower dark grey shading indicates the maximum and minimum allowed within the quoted magnetar distance uncertainties. A 15 per cent error is used where one is not available. The I -band host-normalised offset is shown ($r_e = 3.28$ kpc), similar results are obtained using the B -band r_e of 3.75 kpc (see Table A1 of appendix A). The comparison data are from Mannings et al. (2020, FRBs), Blanchard et al. (2016); Lyman et al. (2017, LGRBs), Fong et al. (2013, SGRBs), Uddin et al. (2020, type Ia SNe), Kelly & Kirshner (2012); Schulze et al. (2020, CCSNe), Lunnan et al. (2015); Schulze et al. (2020, SLSNe), and Lunnan et al. (2017); De et al. (2020b, Ca-rich SNe).

Table 2. Offset and host-normalised offset AD test results, for the comparisons made in Fig. 7. Top: offsets, middle: B -band host normalised offset (the comparison data is also normalised in a UV/blue band where available), bottom: I -band host normalised offset. p-values of 0.05 or greater, indicating statistical consistency, are highlighted in bold and have a grey background. Note that host-normalised data for SNe Ia are not available.

Galactic NS	LGRB	SLSN	CCSNe	FRB	SN Ia	Ca-rich SNe	SGRB
Magnetars	0.00	0.00	0.00	0.07	0.17	0.19	0.00
HMXRBs	0.00	0.00	0.00	0.04	0.02	0.13	0.00
Y. Pulsars	0.00	0.00	0.00	0.03	0.11	0.23	0.00
Pulsars	0.00	0.00	0.00	0.00	0.00	0.01	0.00
LMXRBs	0.00	0.00	0.25	0.25	0.00	0.00	0.00
SNRs	0.00	0.00	0.00	0.25	0.01	0.10	0.00
Magnetars	0.00	0.01	0.00	0.25	n/a	0.02	0.04
HMXRBs	0.00	0.00	0.00	0.25	n/a	0.00	0.01
Y. Pulsars	0.00	0.00	0.00	0.25	n/a	0.01	0.09
Pulsars	0.00	0.00	0.00	0.06	n/a	0.00	0.00
LMXRBs	0.00	0.25	0.00	0.09	n/a	0.19	0.00
SNRs	0.00	0.02	0.00	0.10	n/a	0.01	0.00
Magnetars	0.00	0.00	0.00	0.25	n/a	0.02	0.05
HMXRBs	0.00	0.00	0.00	0.18	n/a	0.00	0.02
Y. Pulsars	0.00	0.00	0.00	0.11	n/a	0.01	0.08
Pulsars	0.00	0.00	0.00	0.02	n/a	0.00	0.00
LMXRBs	0.00	0.25	0.00	0.25	n/a	0.22	0.00
SNRs	0.00	0.00	0.00	0.25	n/a	0.01	0.00

have along their sight-lines, they cannot match the CCSN offset distribution. When calculating the maximum and minimum offsets along a line of sight, the 5 magnetars without distance estimates could also be used. However, their inclusion will add a very limited amount of information - particularly as 4 of the 5 lie on sight-lines close to the Galactic Centre, therefore making a wide range of offsets possible.

Looking at Fig. 7, it is evident that the specific morphology of the Milky Way dictates the shape of the Galactic distributions. The nuclear ring has a high density of magnetars, relative to other arm structures. This is reflected as a dearth of objects at < 3 kpc and a rapid climb in the cumulative distribution at $3-5$ kpc. It is interesting to note that the magnetar locations appear to favour this inner, nuclear ring, over spiral arms further out. This does not appear to be a distance-sensitivity effect as arms at similar heliocentric distances still have fewer magnetars. This may be suggestive of other factors playing a role in their production, beyond a high star formation rate (such as metallicity or IMF variations) and warrants further investigation.

Note that there is an object at a 1.5 kpc Galactocentric offset that has not been included, as it lies just beyond our $y < 8.3$ kpc magnetar cut. It lies in the offset gap (at $\log_{10}(\text{offset/kpc}) = 0.17$), and its inclusion would only increase the similarity to the FRB (and SNR) samples. The known lack of pulsars in the Galactic centre (due to survey biases) means that the actual pulsar distribution is likely less offset. Interestingly, extragalactic CCSNe do not agree well with the SNR distribution (Galactic SNRs are more offset). This could again be due to the specific morphology of the Milky Way, where there is a dearth of young remnants in the older bulge region, a feature not present in every supernova host. Additionally, it could be an artefact of looking at the Milky Way face-on, whereas our views of supernova hosts are at random orientations. SNe at large ($x - y$) Galactocentric offsets can appear to be at low projected offsets, if we are viewing a edge-on disc, for example (Kelly & Kirshner 2012). Overall, this demonstrates that projected offsets are dependent on Galaxy morphology - in particular for the Milky Way, the presence of a nuclear ring of star formation, and a low star formation bulge. Summing across the variety of extragalactic transient hosts and viewing angles, these effects are diluted. Nonetheless, the better agreement of Galactic neutron star distributions with FRBs, compared to other extragalactic transients, is striking.

6 ENCLOSED FLUX

Another way to measure how the neutron stars relate to light is to measure the fraction of the total Galactic flux enclosed at their radial distance. We calculate this for the magnetar, pulsar and XRB samples, and additionally use the SNR radial distribution of Verberne & Vink (2021). The comparison to supernova (Anderson & James 2009; Anderson et al. 2015a) and FRB distributions (Mannings et al. 2020) is shown in Fig. 8. The grey shaded regions are the magnetar uncertainties, calculated in the same way as for the offsets. We again restrict the samples and pixels to $y < 8.3$ kpc, and measure the fraction of flux enclosed in the semicircle produced. For the uncertainties, where this takes us past $y = 8.3$ kpc, the Galactocentric offset is still calculated and the corresponding enclosed flux at that radius in the $y < 8.3$ kpc semicircle is used (i.e., we assume symmetry).

AD-test results are given in Table 3. FRBs are the transient most often consistent with the various neutron star populations, with type Ia supernovae second. The FRBs appear to be a better match than Ia SNe, as the p-values are consistently higher, although the sample size

Table 3. As for Table 2, but for enclosed fluxes. The samples are shown in Fig. 8. Only the I -band is used for a fair comparison to the extragalactic samples.

	Type Ia SNe	FRB	Type II SNe	Type Ibc SNe
Magnetars	0.18	0.25	0.12	0.01
HMXRBs	0.01	0.10	0.01	0.00
Y. Pulsars	0.21	0.25	0.25	0.01
Pulsars	0.14	0.25	0.03	0.00
LMXRBs	0.02	0.25	0.00	0.00
SNRs	0.25	0.25	0.03	0.00

is also smaller, making an interpretation difficult. On the other hand, type Ia supernovae are understood to arise (at least primarily) from white dwarf thermonuclear detonations, so the best matching sample which could plausibly be dominated by neutron star progenitors is the FRBs.

As for the offsets, a lack of pulsars in the Galactic centre is biasing their distribution to large enclosed fluxes. Again, CCSNe do not agree as well as might be expected with the young remnants, although type II SNe do match the magnetars and young pulsars. James & Anderson (2006) found that type II SNe avoid the central regions of their hosts in $H\alpha$ imaging, which might be reflecting a higher incidence of galaxies with older bulge populations, like the Milky Way, in the type II host population. This may partly explain why type II SNe are a better match to the young Galactic neutron stars than type Ibc events, which typically occur at low galactic offsets but in hosts with *young* central stellar populations (Kelly & Kirshner 2012). The remaining differences could plausibly be explained by a range of viewing angles as discussed in the previous section.

Much of the light is concentrated centrally in the bulge (in both bands), a predominantly older population where fewer young neutron stars reside. Consequently, the LMXBs (known to be an older population) appear distributed on the Milky Way's I -band light in a similar way to type Ibc supernovae on their hosts, although this does not imply a connection. There are other Galaxy-specific morphological effects that influence the radial flux profile (e.g. the specific arm locations), and there may also be issues related to faint, halo light that is not detected in extragalactic samples Perets & Beniamini (2021). As we are dealing with just one Galaxy, to disentangle these effects we now look at the fraction of light statistic, which operates on a pixel-by-pixel basis, and can be restricted to sub-regions within the Galaxy.

7 FRACTION OF LIGHT

We now turn to the fraction of light (F_{light} , Fruchter et al. 2006) statistic. To recap, the F_{light} distribution is calculated by ranking host-associated pixels by brightness, and assigning each their value in the cumulative sum, normalised by the total galaxy flux. The brightest pixel therefore has the value 1. Unbiased light tracers sample F_{light} values uniformly, those that are concentrated on brighter regions have a distribution below the 1:1 line. UV/blue bands are assumed to trace young stars and thus star formation, whereas IR/red bands better trace stellar mass.

The fraction of light method has the benefit of being less dependent on host morphology. For example, if a transient occurs on a bright star forming region, but at a large offset from the host centre, both the offset and enclosed flux measurements will indicate a low likelihood of association with star formation/stellar mass (depending on the wavelength). The fraction of flux (or F_{light}) value, however, will assign the proportionate ranking in the distribution of host pixels, ranking it highly, and correctly identifying a close association. It is

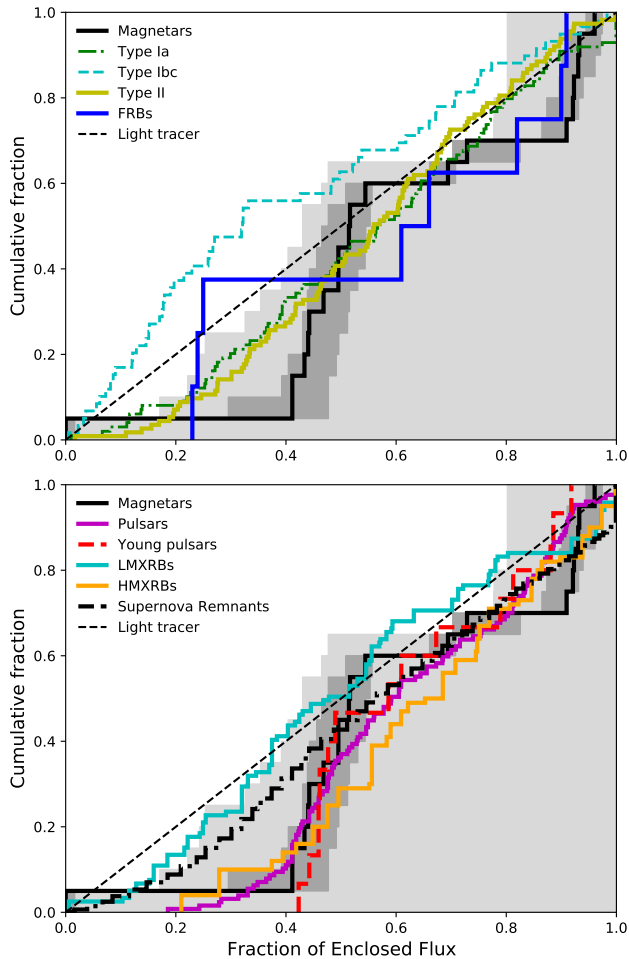


Figure 8. Top: the fraction of Milky Way flux (at $y < 8.3$ kpc) enclosed within the Galactocentric radius of the magnetars, the I -band version is used for a fairer comparison to the extragalactic samples. The maximum and minimum distributions possible for the magnetars are shaded in light grey, the same is shown in dark grey using their given distance uncertainties (or a 15 per cent error where one is not available). The supernovae comparison samples are from Anderson & James (2009) and Anderson et al. (2015b), the FRBs from Mannings et al. (2020). Bottom: enclosed fluxes for the five Galactic samples and the radial SNR distribution.

also possible to restrict the region considered, for example, if we want to look solely at the disc (Lyman et al. 2017). This enables us to probe how transients (or in our case neutron stars) trace light in different stellar populations.

Because F_{light} relies on pixel values, we try 3 different map resolutions - 1000, 500 and 250 pc per pixel. The latter is broadly typical of *HST* resolution for targets at cosmological distances. We initially select all pixels at $y < 8.3$ kpc and within 12 kpc of the Galactic centre as being associated with the galaxy (but the impact of this assumption will be explored).

7.1 Magnetars

As throughout, only magnetars and pixels this side of Galactic centre ($y < 8.3$ kpc) are used. The pixels in the half-Galaxy are ranked by their cumulative value and normalised. The pixel selection, and the 3 image resolutions, are demonstrated in Fig. 9.

The magnetar F_{light} distributions are compared with extragalactic transients in Fig. 10. The light and dark grey uncertainty bands are again derived from the maximum and minimum pixel values possible along the line of sight, and within the quoted distance ranges (or with a 15 per cent distance uncertainty otherwise). Because this can take us past $y = 8.3$ kpc (particularly for the maximum distances along a sight-line), for the uncertainties, we relax the y coordinate restriction on pixel values, and use the whole map (as shown in Fig. 9), including the 30 degree mirrored section.

The dark grey uncertainty band is somewhat larger here than for the offsets or enclosed fluxes. This is because we are now dealing with pixel values, which can have far more variation along the same line of sight than offsets (no dependence on pixel values) or enclosed fluxes (summing pixel values within a radius). We note that, because the quoted uncertainties are typically not formally quantified, we have simply shaded between the upper and lower heliocentric distances (i.e., assuming constant probability density in this range). In reality, the probability density closer to the assumed magnetar distances is likely greater than at the edges of these ranges.

7.2 Fraction of light uncertainties

To create the F_{light} colour maps and distributions in Figs. 9 and 10, we took a 12 kpc Galactocentric pixel selection radius r_{pixel} , and restricted both the pixels and the magnetar sample to $y < 8.3$ kpc to reduce the impact of incompleteness (relaxing the pixel constraint for the uncertainties only). In Fig. 11 we show alternative distributions, first taking pixel selection radii of 10 and 14 kpc instead, and then restricting the areas considered.

The choice of pixel selection radius has only a small impact on the resultant F_{light} values. We next investigate the effect of magnetar sample incompleteness and stochasticity by splitting the Galaxy into three regions, labelled A, B and C in Fig. 11. Region A is the portion of the Galaxy which is (i) within a 5 kpc heliocentric distance and (ii) within a 12 kpc Galactocentric distance, and should in principle be much less affected by both neutron star and maser sample incompleteness effects. This also allows us to examine the relationship between the magnetars and spiral arms without the influence of the bulge, which is a different, older stellar population. Regions B and C move this region around the Galaxy. We avoid a fourth region, which would be region A but mirrored over Galactic centre, because the maser positions here are arbitrary (see Section 3). The F_{light} distributions of regions A, B and C are shown in the lower panels of Fig. 11. We have combined regions B and C due to the lower number statistics, and the fact that these regions are equidistant from both our location and Galactic centre. For regions B and C, we remove the $y < 8.3$ kpc requirement for both the magnetars and the pixels. These regions show a stronger correlation with light, but extend to larger heliocentric distances, so the influence of incompleteness effects cannot be ruled out in shaping these distributions. For regions A, B and C, both the sample objects and pixels are restricted to this area, F_{light} is recalculated using these pixels only, and we do not consider objects that fall outside.

Restricting the F_{light} analysis to the local disc has a larger impact in the I -band than the B -band. This makes sense for the magnetars, as they are already preferentially sampling the star-forming disc, so restricting ourselves to the local 5 kpc has a small impact. Conversely, the magnetars appear to avoid I -band light when the bulge is considered, so removing its contribution increases the correlation with light, as expected. For the interested reader, we have made python

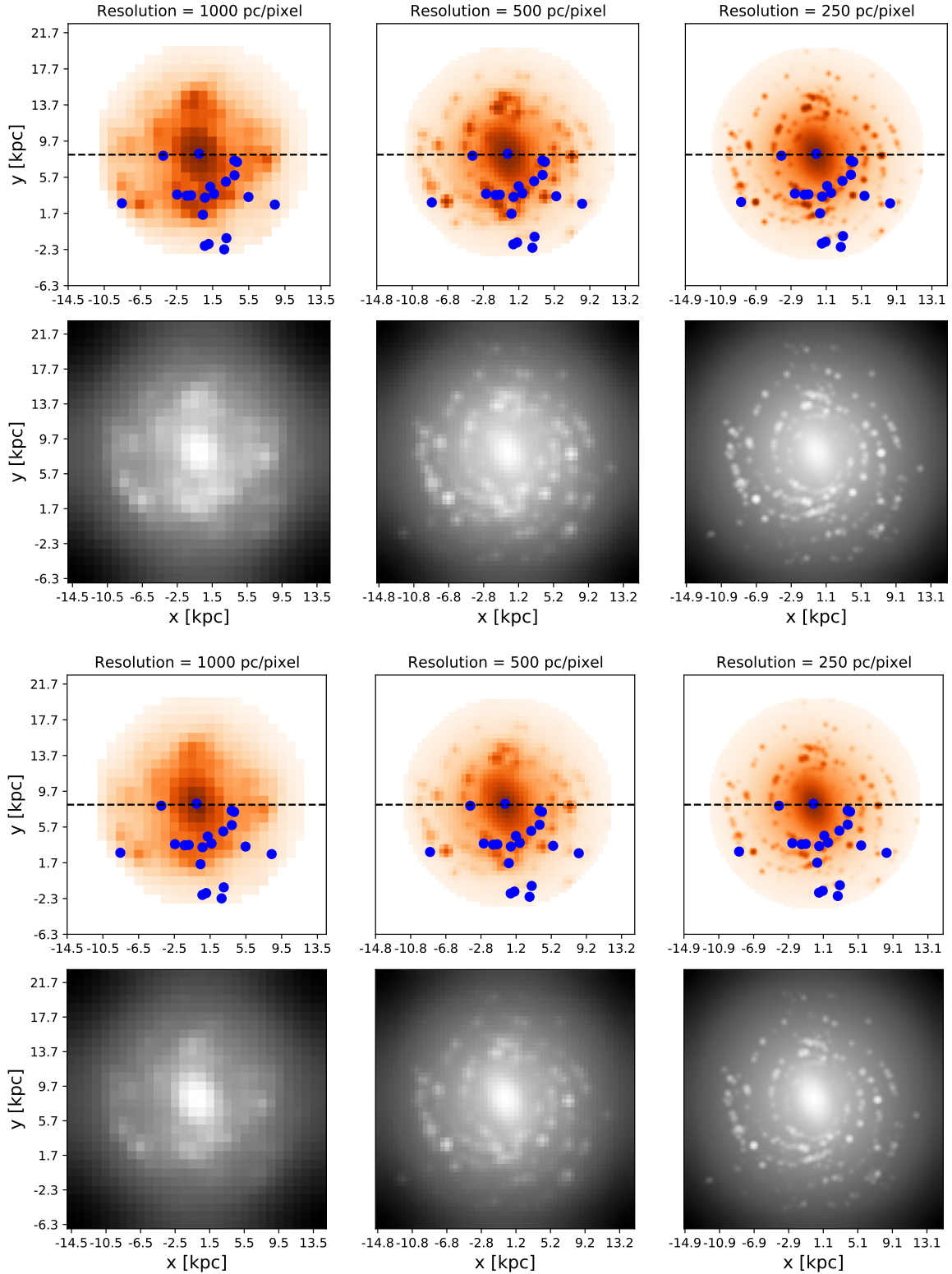


Figure 9. F_{light} colour maps (orange) with magnetars at $y < 8.3$ kpc overlaid, and Milky Way image stamps (grey, logarithmic scaling) at 3 spatial resolutions (1000, 500 and 250 pc/pixel). The B -band is shown in the upper two rows, the I -band in the lower two. The 250 pc/pixel scale (with a 2 pixel FWHM) is broadly representative of *HST* spatial resolution for cosmological transients. Pixels within a 12 kpc Galactocentric radius at $y < 8.3$ kpc (i.e., below the dashed horizontal line) are selected for calculating F_{light} distributions. However, we show the whole F_{light} colour map here, as the $y > 8.3$ kpc area is used when considering the full range of F_{light} values that are possible along each sight-line, or within the magnetar distance uncertainties.

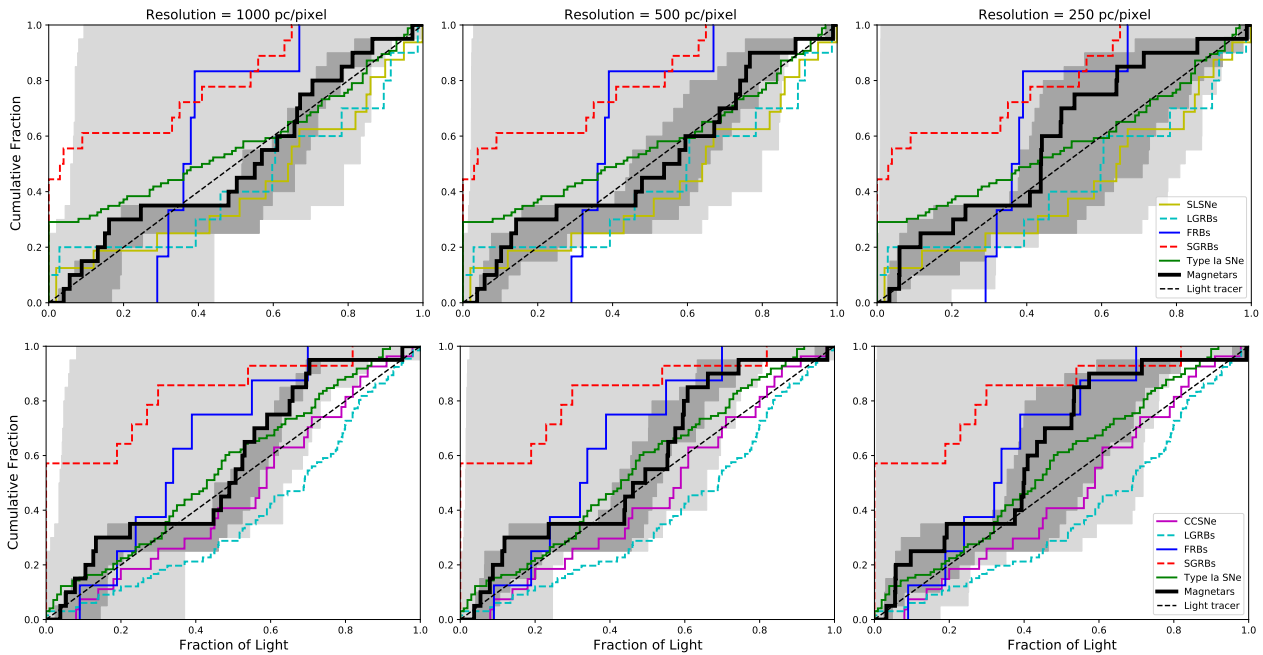


Figure 10. *B*-band (top) and *I*-band (bottom) fraction of light distributions for the magnetars in the Milky Way, viewed face-on. For the magnetar distributions (solid black lines), pixels less than 12 kpc from GC, and this side of GC, were considered associated. The light grey shaded regions represent the minimum and maximum distributions that arise from taking the minimum and maximum F_{light} values along the magnetar sight-lines, for which we relax the $y < 8.3$ kpc restriction. This places a strong upper limit on how concentrated magnetars can be on the Galactic light. The darker grey bands use linear sampling between the McGill catalogue upper and lower distance estimates, taking the mean uncertainty of 15 per cent on a distance where a range is not provided (again, the whole image is used, in case the error bars take us past $y = 8.3$ kpc). The distributions for various extragalactic transients on their host galaxies are also shown. These samples are from Mannings et al. (2020, FRBs), Blanchard et al. (2016); Lyman et al. (2017, LGRBs), Fong et al. (2013, SGRBs), Wang et al. (2013, type Ia SNe), Svensson et al. (2010, CCSNe), Lunnan et al. (2015, SLSNe).

scripts and notebooks available which generate a similar F_{light} figure, given user defined input parameters³.

7.3 Pulsars and XRBs

The method described for the magnetars is repeated for the ATNF luminous pulsars and the INTEGRAL XRBs. Their positions on the half-map, the three sub-regions, and the resultant F_{light} distributions, are shown in Figs. 12, 13 and 14. For regions A, B and C, F_{light} is recalculated using these pixels exclusively, and objects that fall outside are not included. For the half-Galaxy, objects outside the 12 kpc Galactocentric radius are considered, and are assigned an F_{light} value of 0.

In Fig. 12, as regions A, B and C avoid the Galactic centre, the effect of there being a detection bias against pulsars in the GC is much reduced. The result of varying the pulsar luminosity cut is also demonstrated. Moving the cut within the region denoted by the dashed lines in Fig. 2, the maximum and minimum distributions that occur in this range are shaded between in Fig. 12. Lower cuts bias the sample to lower heliocentric distance, increasing the relative contribution of the Galactic bulge and thus increasing F_{light} .

The young pulsar distribution in F_{light} follows the wider pulsar sample. A similar result was found in the offsets and enclosed fluxes. The younger pulsars (age $< 10^5$ yr) should in principle trace the magnetars more closely - however it isn't clear whether they truly have a comparable age distribution. The difference could also arise

due to differences in distance measurements (i.e. the pulsar distances are predominantly inferred from dispersion measures). If this result is real however, it might imply that magnetars and pulsars have different evolutionary histories (a possibility that will be explored further in paper II).

As for the magnetars, restricting the area to the disc pushes the pulsar and HMXBs distributions closer towards the 1:1 line, with the effect greater in the *I*-band than the *B*-band. Again, this is because these samples avoid the Galactic bulge (due to survey/detection biases, at least in the pulsar case). The opposite occurs for LMXBs, which being an older population, already favour the Galactic bulge. As a result, restricting the analysis to the disc pushes them away from the 1:1 line, and more so in the *B*-band than the *I*-band. This has important ramifications for the use of F_{light} , which we will explore in the discussion.

7.4 Fraction of light results

Taking our half-Galaxy pixel map with a 12 kpc radius (for the best comparison with extragalactic samples), AD tests between the magnetars/pulsars/XRBs and extragalactic transients are listed in Tables 4 and 5.

Across the five Galactic samples and across all three resolutions, as we found for the offset and enclosed flux measurements, FRBs most frequently do not reject the null hypothesis that they are drawn from the same distribution as Galactic neutron stars. They are more clearly the preferred transient when looking at the *I*-band results. The uncertainties are generally larger in the *B*-band (this can be seen in Fig. 10), because the arms contribute a higher fraction of the total

³ <https://github.com/achrimes2/MW-NS-Flight>

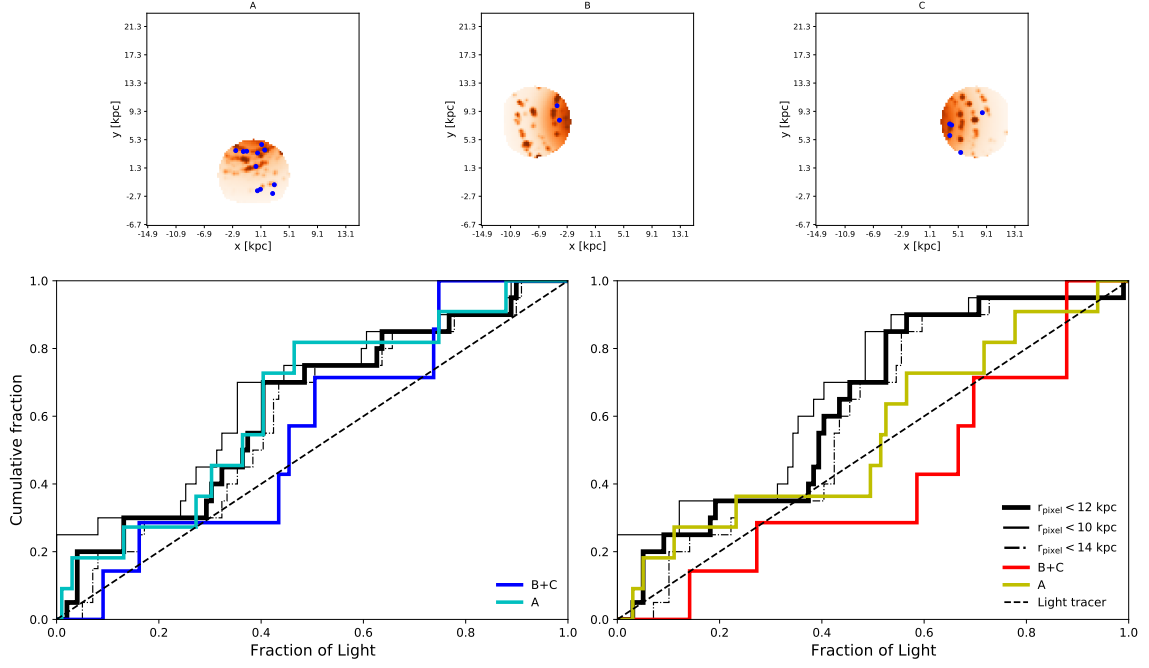


Figure 11. Exploring the effects of incompleteness and choices of methodology on the magnetar F_{light} distributions. Top: the pixel selection for F_{light} when a 5 kpc heliocentric distance restriction is applied. Region A uses our actual location within the Galaxy, B and C explore the effects of incompleteness and stochasticity (the $y < 8.3$ restriction is relaxed for regions B and C). Only the B -band version is shown for brevity. Bottom: magnetar F_{light} distributions calculated in different ways (B -band left, I -band right), to demonstrate the effects of uncertainties and choices of methodology. Regions A and B+C are shown, where B and C are combined due to avoid low numbers. The thick black lines are the magnetar distributions with the standard setup of using magnetars and pixels at $y < 8.3$ kpc, with pixels less than 12 kpc from GC used in the F_{light} cumulative sum. The thin and dashed black lines show the effect of choosing different pixel selection radii. In all cases an image resolution of 250 pc/pixel is used.

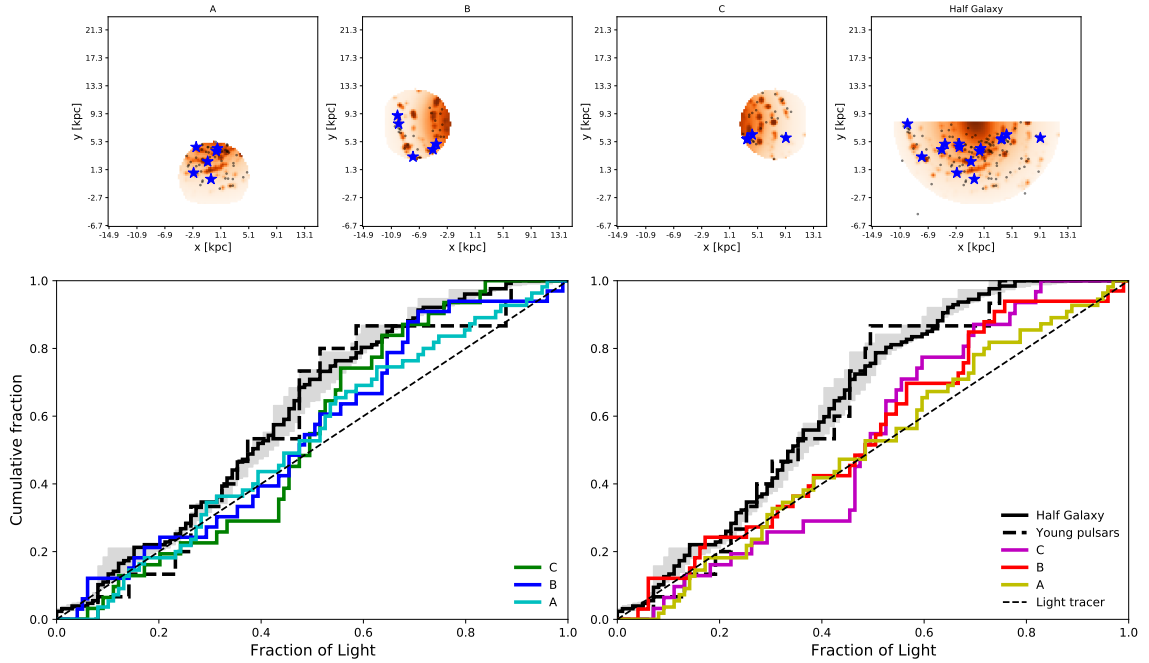


Figure 12. The same information as in Fig. 11, but for the bright ANTF pulsars. The $< 10^5$ yr subsample (for which the whole Galaxy distributions are shown) is marked by stars, the half-Galaxy sample by dots. Top: the B -band pixel selection for pulsar F_{light} when a 5 kpc heliocentric distance restriction is applied, and the pixels and pulsars used for the half-Galaxy distribution. Bottom: F_{light} for the half-Galaxy, regions A, B and C, and the half-Galaxy young pulsars (B -band left, I -band right). The grey shading bounds the minimum and maximum distributions that arise from varying the luminosity cut by ± 0.5 dex (see Fig. 2). Only in the half-Galaxy case do we consider pulsars outside the selected pixels, assigning them $F_{\text{light}} = 0$.

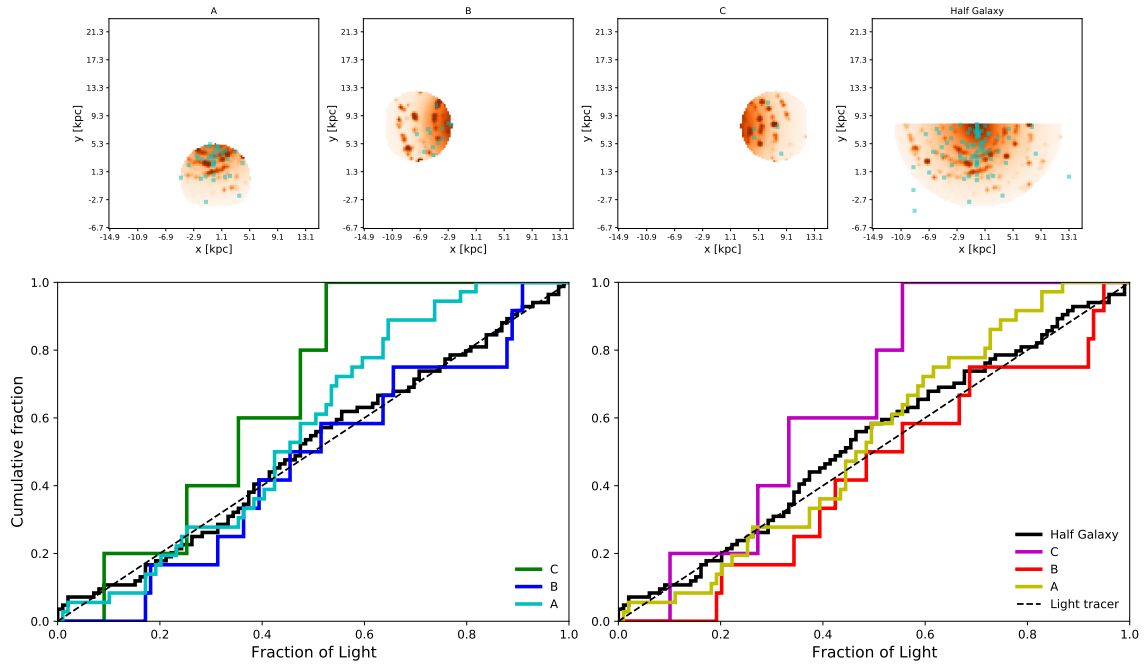


Figure 13. The same information as in Figs. 11 and 12, but for the LMXBs. Top: the B -band pixel selection for LMXB F_{light} when a 5 kpc heliocentric distance restriction is applied, and the pixels and XRBs used for the half-Galaxy distribution. Bottom: F_{light} for the half-Galaxy, and regions A, B and C (B -band left, I -band right).

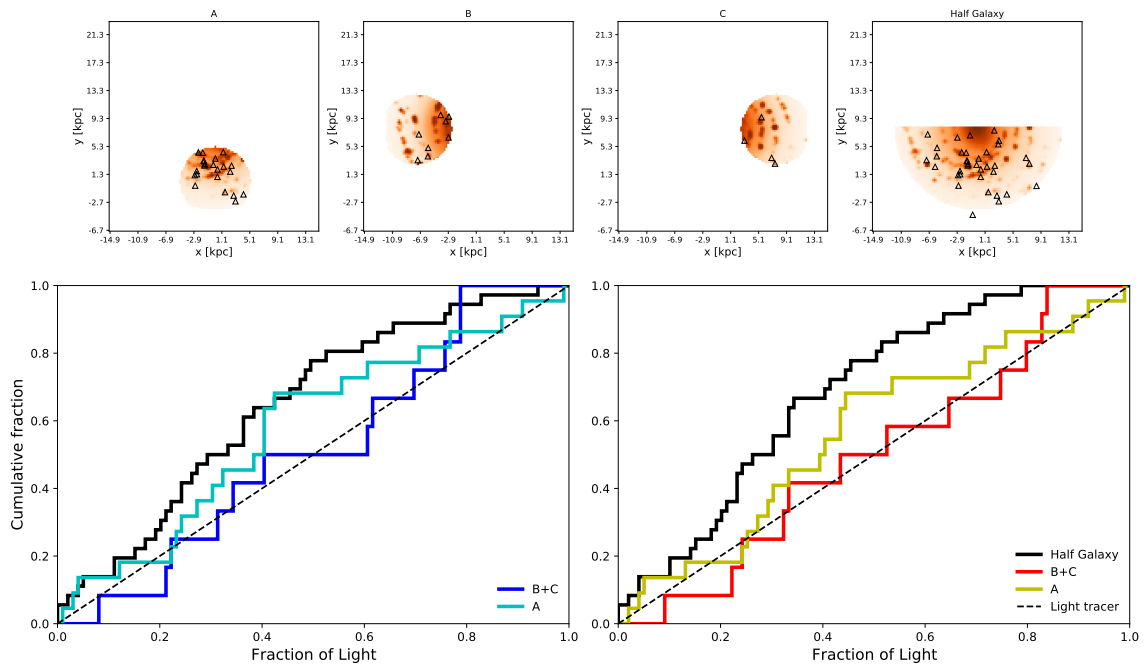


Figure 14. The same information as in Figs. 11, 12 and 13, but for the INTEGRAL high-mass X-ray binary sample of Kretschmar et al. (2019). Top: the B -band pixel selection for HMXB F_{light} when a 5 kpc heliocentric distance restriction is applied, and the pixels and XRBs used for the half-Galaxy distribution. Bottom: F_{light} for the half-Galaxy, and regions A, B and C (B -band left, I -band right). As in Fig. 11, regions B and C have been combined, as there are only 4 XRBs in region C. B -band values are shown on the left, I -band on the right.

Table 4. As for Tables 2 and 3, but for B -band (half Galaxy) F_{light} comparisons, as shown in Figs. 10 (and 11), 12, 13 and 14. Top: Milky Way image resolution of 250 pc/pixel, middle: 500 pc/pixel, bottom: 1 kpc/pixel.

	LGRB	SLSN	FRB	SN Ia	SGRB
Magnetars	0.18	0.09	0.25	0.04	0.00
HMXRBs	0.03	0.01	0.25	0.01	0.00
Y. Pulsars	0.10	0.07	0.25	0.05	0.00
Pulsars	0.01	0.00	0.25	0.00	0.00
LMXRBS	0.25	0.25	0.22	0.00	0.00
Magnetars	0.25	0.25	0.14	0.06	0.00
HMXRBs	0.09	0.03	0.25	0.01	0.00
Y. Pulsars	0.16	0.13	0.25	0.07	0.00
Pulsars	0.02	0.01	0.25	0.00	0.00
LMXRBS	0.25	0.25	0.07	0.00	0.00
Magnetars	0.25	0.25	0.18	0.05	0.00
HMXRBs	0.17	0.09	0.21	0.02	0.00
Y. Pulsars	0.19	0.18	0.23	0.04	0.00
Pulsars	0.06	0.03	0.20	0.00	0.00
LMXRBS	0.25	0.25	0.03	0.00	0.00

Table 5. As for Tables 4, but for I -band (half Galaxy) F_{light} comparisons, as shown in Figs. 10 (and 11), 12, 13 and 14. Top: Milky Way image resolution of 250 pc/pixel, middle: 500 pc/pixel, bottom: 1 kpc/pixel.

	LGRB	CCSNe	FRB	SN Ia	SGRB
Magnetars	0.00	0.02	0.25	0.25	0.00
HMXRBs	0.00	0.00	0.25	0.02	0.00
Y. Pulsars	0.00	0.05	0.25	0.25	0.00
Pulsars	0.00	0.00	0.25	0.00	0.00
LMXRBS	0.00	0.25	0.25	0.25	0.00
Magnetars	0.00	0.11	0.25	0.25	0.00
HMXRBs	0.00	0.00	0.25	0.09	0.00
Y. Pulsars	0.00	0.10	0.25	0.25	0.00
Pulsars	0.00	0.00	0.25	0.01	0.00
LMXRBS	0.05	0.25	0.11	0.08	0.00
Magnetars	0.01	0.14	0.25	0.25	0.00
HMXRBs	0.00	0.02	0.25	0.25	0.00
Y. Pulsars	0.00	0.09	0.25	0.25	0.00
Pulsars	0.00	0.01	0.25	0.07	0.00
LMXRBS	0.25	0.25	0.04	0.00	0.00

Table 6. AD-test F_{light} results for comparisons with region A only (Figs. 11, 12, 13 and 14), where biases and uncertainties in both the map and Galactic samples are much reduced. Top: B -band, bottom: I -band. Only the high-resolution, 250 kpc/pixel results are shown. The decrease in mapping uncertainties and incompleteness is counteracted by a decreased sample size, so that the AD-tests return similar results.

	LGRB	SLSN	FRB	SN Ia	SGRB
Magnetars	0.25	0.22	0.25	0.18	0.01
HMXRBs	0.25	0.25	0.25	0.25	0.07
Y. Pulsars	0.25	0.25	0.25	0.13	0.01
Pulsars	0.19	0.09	0.07	0.01	0.00
LMXRBS	0.25	0.18	0.25	0.25	0.07
	LGRB	CCSNe	FRB	SN Ia	SGRB
Magnetars	0.13	0.25	0.25	0.25	0.00
HMXRBs	0.01	0.18	0.25	0.25	0.00
Y. Pulsars	0.25	0.25	0.22	0.08	0.00
Pulsars	0.02	0.25	0.22	0.22	0.00
LMXRBS	0.00	0.25	0.22	0.25	0.00

flux. Random variations in location due to distance uncertainties therefore sample a wider range of pixel values along a given line of sight, providing a wider range of possible distributions.

As we saw for the Galactocentric offsets, CCSNe are not in good agreement (they are more concentrated on their host light than Milky Way neutron stars), and SGRBs are the least consistent with Galactic neutron star populations (they are less concentrated). The former result implies one, or a combination, of the following: (i) neutron star natal kicks are driving this difference, although even the young magnetars are inconsistent, (ii) spatial resolution effects are playing a role, such that CCSN offsets from brighter regions are not being resolved in imaging, (iii) there are real differences between supernova locations in the Milky Way and other galaxies or (iv) neutron star distance uncertainties are scattering them away from their true (brighter pixel) locations/maser incompleteness is artificially reducing the relative pixel brightness at the neutron star location. To address the latter concern, we now examine results from region A of Figures 11, 12, 13 and 14.

7.5 Region A comparisons

In Sections 2 and 3, we applied corrections to account for incompleteness at large heliocentric radii, both in terms of the star forming region masers and the magnetars/pulsars/XRBs. Although we also restricted much of the analysis to $y < 8.3$ kpc to reduce these issues, some still remain. For example, the masers were not well corrected for on longer length scales (the inter arm regions). The magnetars are less likely to be detected at greater distances (Fig. 1), while there is a distinct absence of pulsars around the Galactic centre, due to survey biases (Rajwade et al. 2017, and Fig. 2). The XRBs should in theory be less biased given the survey detection limits (Krivonos et al. 2017, and Section 2), however it is difficult to tell whether this is truly the case. In summary, our half-Galaxy comparisons to extragalactic samples may be suffering from biases which have not been fully corrected.

In order to quantify the effect these biases have on our results, we present AD-test results for region A versus extragalactic transient samples. These regions (within 5 kpc of our location) are sufficiently local that the aforementioned biases will be much reduced. Furthermore, distance uncertainties tend to be lower in this region (for example, trigonometric parallax measurements have made in several cases).

Table 6 gives the region A test results. The results are less clear compared to the half-Galaxy comparisons. FRBs are frequently a good match to Galactic neutron stars, and the significance of this is even more apparent when the p-values are considered (reaching the 0.25 cap 4/5 times). However, unlike the half-Galaxy case, LGRBs, SLSNe and CCSNe are also consistent with each Galactic population. Plausibly, the smaller sample sizes that result from restricting ourselves to < 5 kpc reduce the power of the AD-test, making consistency with other samples harder to rule out. Nonetheless, the result that FRBs locations on their hosts are consistent with Galactic neutron star locations seems to be robust against incompleteness effects. Although Galactic neutron stars do appear to match FRBs well in terms of F_{light} , we are unable to clearly differentiate which classes of neutron star are most likely to be the progenitors.

8 DISCUSSION

We now discuss our findings, grouping them into three areas: the results and their significance, the implications for the use of F_{light} , and implications for progenitors of fast radio bursts.

8.1 Summary of results and their significance

8.1.1 Summary of results

We give an overview of our results, in terms of the percentage of times that different extragalactic transients agree at the 2σ level with Galactic neutron stars, as measured on the Milky Way face-on image. To do this, we split the Galactic populations into ‘young’ remnants (magnetars, young pulsars, HMXBs and SNRs) and ‘old’ (LMXBs, pulsars). The comparisons considered are the Galactocentric offsets and host-normalised offsets in both bands, the I -band enclosed flux, the B and I half-Galaxy F_{light} and region A (disc only, but more complete) B and I F_{light} . For F_{light} , only the highest spatial resolution is used. For each extragalactic transient, we count how many AD-test comparisons have been made in total, and how many resulted in $p > 0.05$. The percentage of ‘successful’ tests, indicating consistency, is shown in Fig. 15.

It is clear from this summary figure that the distribution of Galactic neutron stars on the Milky Way best matches, of all of the transients, FRBs on their hosts. However, we are unable to differentiate which classes of neutron stars are the best fit. Of the other samples, SGRBs (known to be mergers involving at least one neutron star, Barthelmy et al. 2005; Fong et al. 2010; Church et al. 2011; Tunnicliffe et al. 2014; Abbott et al. 2017), are the worst match. SRGBs have extended offset distributions, due to the combination of natal kicks and long gravitation wave inspiral times. The implication is that, in the Milky Way, old, kicked systems are missing from our catalogues, possibly because they are distant and not bright emitters like magnetars, pulsars or XRBs. Type Ia SNe are the clearest second best match, for ‘young’ systems at least. The frequent agreement of SNe Ia with young Galactic neutron stars may be reflecting the presence of short-delay time channels in the type Ia SN population (e.g. Castrillo et al. 2021, who find Ia delay times with a 50 per cent confidence interval of 50^{+100}_{-35} Myr). While the majority of SNe Ia are thought to arise from white dwarf thermonuclear detonations, there are also models for the accretion-induced collapse of white dwarfs into magnetars, which may be accompanied by supernova-like ejecta and emission (Lyutikov & Toonen 2019). Of the other samples, none stand out as being more or less consistent with the Galactic populations.

8.1.2 Neutron star and Galaxy mapping uncertainties

We now consider the effect that distance uncertainties in the magnetar/pulsar/XRB samples have on our results. It is possible that the neutron star F_{light} distributions are artificially less concentrated with respect to light due to distance uncertainties, which are scattering them off the brighter maser-dense regions. If this were the case, it follows that the brighter pixels should still lie along that line of sight. We see this behaviour for the magnetars in Fig. 10, where the uncertainties in the B -band are larger, because the light is more concentrated in the clumpy arms (in other words, there is more variation along a sight-line). Based solely on the B -band F_{light} results it is possible that the magnetars actually lie on highly-ranked pixels and are not inconsistent with, for example, long GRBs, however the I -band uncertainties are more constraining, suggesting that the magnetars are more offset from star formation than CCSNe.

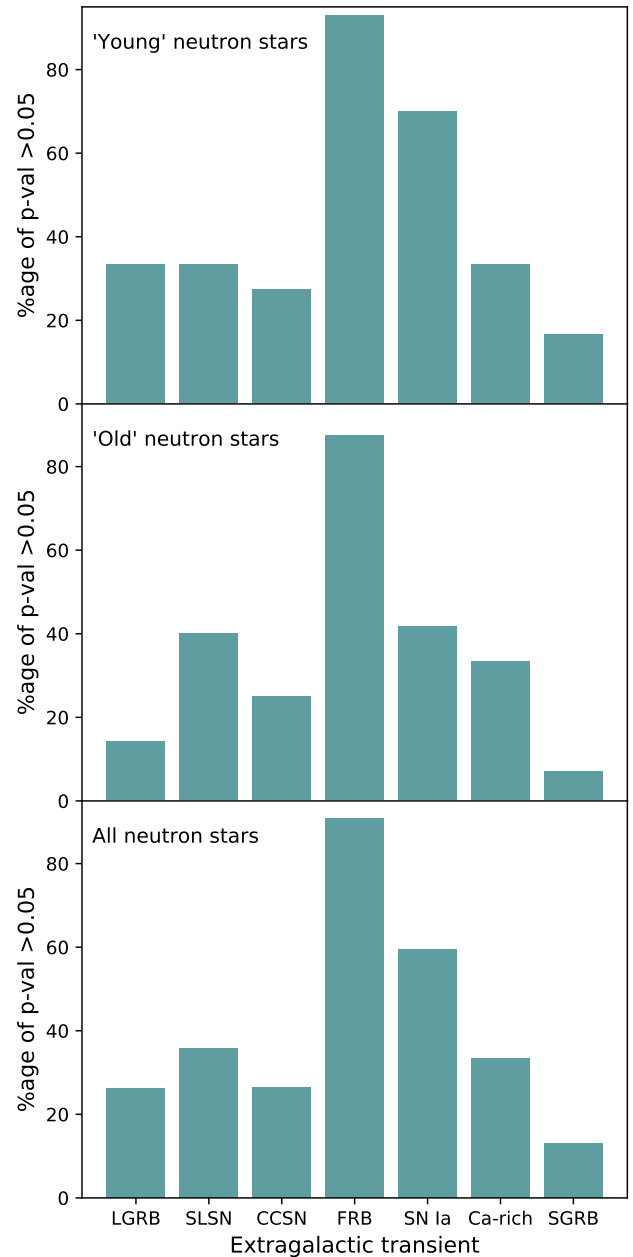


Figure 15. The percentage of AD-test results from throughout this paper with p-values exceeding 0.05, for each of the extragalactic transients, compared with the Milky Way neutron stars. Measurements used are the Galactocentric offset, host-normalised offset, I -band enclosed flux, whole Galaxy F_{light} , and F_{light} within a 5 kpc heliocentric distance. The ‘young’ neutron stars include magnetars, pulsars with age $< 10^5$ yr, HMXBs and SNRs. ‘Old’ neutron stars are pulsars and LMXBs. There is no clear difference between the old and new samples, but overall, FRBs are clearly distributed on their hosts in a similar manner to neutron stars on the Milky Way.

Although distance uncertainties might be making the Galactic populations appear less correlated with masers/star forming regions/spiral arms and therefore light, in Section 4 we showed that offsets from star forming regions of a few hundred parsec are typical for young neutron stars. While lower magnetar offsets cannot be ruled out due to their large distance uncertainties, the HMXB results

are in good agreement with studies measuring their correlation with star forming complexes (e.g. Coleiro & Chaty 2013, who find offsets of ~ 300 pc are typical). If the young neutron star offsets are real, then we must ask why CCSN distributions do not also follow this trend (in terms of e.g. F_{light}). Taking the lower end of the magnetar offsets allowed within the uncertainties, this would tend to place them within the same 250 pc pixel as the nearest maser/star forming region, thus increasing their association with light. This would not, however, explain the discrepancy between SNRs and CCSNe (in terms of Galactocentric offsets and enclosed fluxes), although the specific morphology of the Milky Way and the orientation of our map could explain this, as previously discussed.

If we argue that the magnetars (and other neutron stars) appear less concentrated on the light because distance uncertainties have scattered them away from their actual locations in star forming regions, then reducing the spatial resolution will once again put the brighter regions in the same pixel as the neutron star, because any offsets cannot be resolved. We see this in Fig. 10, where magnetars are closer to being light tracers at 500 pc/pixel and 1 kpc/pixel resolution. However, the AD test results in Tables 4 and 5, demonstrate that even at 1 kpc/pixel resolution, FRBs are still the most consistent with Galactic neutron stars.

An alternative explanation for the weak neutron star relationship with light could be that the arm positions are inaccurate. However, a reason to suspect that arm position inaccuracies are not driving these results is that broadly similar results are again obtained within region A, where the maser distances (and resulting arm model, Reid et al. 2016) are largely derived directly from trigonometric parallax measurements. The other assumptions we have made about the Galactic structure and the colour of the different components also contribute uncertainty, however this appears to be less important than other factor like incompleteness and distance uncertainty. We refer the reader to the interactive tools at <https://github.com/achrimes2/MW-NS-Flight>, which can be used to vary the relative light contributions of the bulge/bar, disc and arms, to visualise the impact on F_{light} .

8.2 Implications for use of the fraction of light

In F_{light} studies, blue bands (e.g. the B -band) are often used as a tracer of star formation, while red/NIR bands are used for stellar mass. In disc-and-bulge spirals like the Milky Way, we could naively therefore expect mass-tracing events to prefer the bulge, and star-formation tracers to prefer the disc. However, we do not see such a clear delineation between the B and I -band distributions we have constructed. This is in part because the radial light profiles in these bands are similar: their relative strengths vary with radius (with B contributing more in the disc versus the bulge), but B -band pixel values in the bulge are typically higher than B -band pixel values in the disc. This arises simply because in *both* bands, the disc is defined by the same exponential disc profile, such that the inner regions will always be brighter. This partly explains why systems we know to be old, such as LMXBs, appear to trace *blue* light more strongly than young magnetars. We therefore caution that F_{light} measurements in galaxies which clearly have multiple, overlapping structural components should be carefully handled. Comparisons should ideally be between similar galaxy types, and where this is not possible, between similar components within them (e.g. spiral galaxy bulges versus ellipticals).

The effect of considering just one component of the Galaxy is demonstrated best by the B -band region A comparisons in Figs. 11, 12, 13 and 14. LMXBs become more weakly correlated with light when restricted to the star forming disc. The fact that the increase in

correlation with light for magnetars, HMXBs and pulsars is less in the B -band than the I -band could be the manifestation of a dearth of these samples in the Galactic bulge to start with (as we were already preferentially sampling the disc), whether or not this is real or result of biases, as is well understood in the pulsar case. We can also see from Fig. 10 and our discussion in the previous subsection that high spatial resolutions are necessary for F_{light} to be a useful tool. This highlights an ongoing need for *HST*-like high-resolution, UV capability, and suggests that the physical scale of the imaging used should be considered when performing F_{light} comparisons between transients.

In constructing the Galaxy images, we assumed that the spiral arms contribute 20 per cent of the disc's B -band light. If B -band light is used as a star formation tracer, then we should expect only ~ 20 per cent of the magnetars (and other young systems) to be associated with spiral arms. However, in Figs. 4 and 9, they are clearly more correlated than this. This results arises because the B -band is a good tracer of rest-frame UV emission at redshifts of > 1 , whereas our Milky Way measurements are at $z = 0$, and the UV is a better tracer of ongoing star formation than the B -band. For reference, see the discussion in Section 3 regarding the maser map similarity to UV imaging of other spiral galaxies. This demonstrates that the redshift range should also be considered when performing F_{light} comparisons. While this implies that our Galactic samples should appear less correlated with star formation than they would at cosmological distances in the same band, our FRB comparisons are relatively unaffected by this difference, as they all lie at redshift $z < 0.7$. We note that using a better tracer of star formation would also reduce the LMXB correlation with B -band light, which does not represent a genuine strong association with young stars as previously discussed.

Another way to detect and isolate ongoing star formation, with reduced continuum contamination, is to employ $H\alpha$ imaging, which has previously been done for CCSNe (James & Anderson 2006; Anderson & James 2008; Anderson et al. 2012a). Interestingly, pixel statistic studies of CCSN locations on $H\alpha$ host imaging have shown that around 40 per cent of type II SNe occur in pixels which are *faint*, relative to the rest of the host (James & Anderson 2006). It has been suggested that their progenitors are 'runaway' stars, ejected from their birth sites, which would travel up to ~ 100 pc before going supernova (Eldridge et al. 2011). Type II SNe are less concentrated on their host $H\alpha$ light than type Ibc SNe, which has been ascribed to greater type Ibc progenitor masses, and hence shorter lifetimes (James & Anderson (2006); Anderson & James (2008); Anderson et al. (2012a)). However, the significance of this is unclear, as a similar effect could arise if type II progenitors outlive their natal HII region (Crowther 2013). Nevertheless, we note that offsets of ~ 100 parsec are similar to those we and other studies have found for young neutron star systems. A full exploration of the nature of the young neutron star-star forming region offsets is beyond the scope of this paper, but we will return to these questions in paper II.

8.3 Implications for the magnetar-FRB connection

Initial FRB host population studies (Heintz et al. 2020; Mannings et al. 2020) led to differing interpretations over whether magnetar flares can explain all FRBs (Bochenek et al. 2020a; Safarzadeh et al. 2020; Margalit et al. 2020). It is also unclear whether the identification of FRB-like flares from SGR 1935 (Bochenek et al. 2020b; CHIME/FRB Collaboration et al. 2020) definitively establishes a connection between magnetars and extragalactic FRBs (Tavani et al. 2021; Ridnaia et al. 2021; Bailes et al. 2021).

Our results, looking at Milky Way magnetar, pulsar and XRBs on the Milky Way’s light, show that Galactic neutron stars are consistent with FRB locations on their hosts. This result holds regardless of the type of comparison made (distance to the star forming region, host offset, enclosed flux and fraction of light), although the significance varies substantially between these and the specific Galactic population being compared. Other extragalactic transients are also consistent with the Milky Way neutron star distribution, depending on the comparison made, but FRBs are the transient most frequently in agreement. However, our results cannot differentiate between various FRB progenitor models which invoke neutron stars (e.g. magnetars from core-collapse and accretion induced collapse, ultra luminous X-ray binaries, combing models etc, [Margalit et al. 2019](#); [Ioka & Zhang 2020](#); [Sridhar et al. 2021](#); [Zhao et al. 2021](#)), but we have shown that ~ 0.1 - 1.0 kpc star forming region-FRB separations do not preclude a magnetar origin.

As a final point, we acknowledge that the FRB host sample is currently small and therefore statistical consistency with other data by means of an AD-test is more likely (or rather, it is harder to rule out). This does not diminish the results summarised in Fig. 15, but reflects the limitations of the current datasets. Looking solely at Fig. 15, neutron star systems appear to be a more plausible origin for FRBs than for other transients (if we were to ignore all other knowledge that we have about the nature of the other transients). To increase the significance of this study’s results, we require better accuracy and precision in Galactic neutron star distance measurements, a deeper understanding of the biases affecting these samples, and a larger sample of FRB hosts. In future, it may be possible to use these methods to determine not only whether extragalactic FRBs arise from neutron stars, but which specific systems are the progenitors.

9 CONCLUSIONS

Motivated by the possibility that magnetar activity is the origin of fast radio bursts, we have created an image of the Milky Way, simulating its face-on appearance from an extragalactic distance. We then placed magnetar, pulsar and XRB populations on the image, according to their best distance estimates, and measured how these systems are distributed with respect to Galactic light. These distributions were then compared to samples of extragalactic transients, including fast radio bursts. Our three main conclusions are summarised below,

- Galactic neutron stars are distributed on the Milky Way in a similar manner to FRBs on their hosts, in terms of Galactocentric offsets, host normalised offsets, enclosed fluxes and F_{light} . FRBs are in better agreement with these Galactic systems than other extragalactic transients. The results appear robust against incompleteness effects, and provide further evidence that FRBs have their origin in neutron star systems. However, we cannot distinguish whether isolated magnetars or accreting/interacting binaries containing a neutron star are the best match,
- Magnetars can be offset by as much as hundreds of parsec from their likely birth sites in the spiral arms, assuming a core-collapse origin. This is in agreement with both type II supernovae locations and FRB offsets from star forming regions within their hosts,
- We argue that galaxy components (i.e. the bulge or disc) should be considered when using the fraction of light diagnostic, because the use of different bands, i.e. a blue filter and a red filter, does not perfectly separate star formation and stellar mass. We also show that similar rest-frame wavelengths should be compared, and that the physical scale of the imaging can have a significant impact on the

resultant distributions, particular if there are structures such as spiral arms with small spatial scales.

We plan to further explore the relationship between compact objects and Galactic structures, and the implication for their progenitor channels and kick velocities, in a future paper. To make further progress with this method for understanding FRBs, improvements in the completeness of Galactic neutron star samples is required, along with decreased heliocentric distance uncertainties. A larger FRB host sample is also needed, but this population will surely grow over the coming years.

ACKNOWLEDGEMENTS

AAC is supported by the Radboud Excellence Initiative. AJL has received funding from the European Research Council (ERC) under the European Union’s Seventh Framework Programme (FP7-2007-2013) (Grant agreement No. 725246).

This work has made use of IPYTHON ([Perez & Granger 2007](#)), NUMPY ([Harris et al. 2020](#)), SCIPY ([Virtanen et al. 2020](#)); MATPLOTLIB ([Hunter 2007](#)) and ASTROPY,⁴ a community-developed core Python package for Astronomy ([Astropy Collaboration et al. 2013](#); [Price-Whelan et al. 2018](#)). We have also made use of Ned Wright’s cosmology calculator [Wright \(2006\)](#).

DATA AVAILABILITY

The input masers used in this paper were selected from the RMS survey ([Urquhart et al. 2014](#)). Their distances were calculated using version 2 of the parallax-based BeSSel ([Brunthaler et al. 2011](#)) distance calculator ([Reid et al. 2016, 2019](#)), available at <https://bessel.vlbi-astrometry.org/node/378>. Neutron star data were obtained from the McGill catalogue (for magnetars, [Olausen & Kaspi 2014](#)), available at <https://www.physics.mcgill.ca/~pulsar/magnetar/main>; the ANTF database (for pulsars, [Manchester et al. 2005](#)), available at <https://www.atnf.csiro.au/research/pulsar/psrcat>; [Sazonov et al. \(2020\)](#), for LMXBs) and [Kretschmar et al. \(2019\)](#), for HMXBs).

We have made interactive python scripts and notebooks available online, which generate the F_{light} results presented in this paper, but also allow the user to change various parameters. These can be accessed at <https://github.com/achrimes2/MW-NS-Flight>. Also available in this repository are the F_{light} , offset and enclosed flux values for the magnetar, pulsar and XRB samples used in this paper. These data can also be found on the journal website as supplementary materials.

REFERENCES

- Abbott B. P., et al., 2017, *ApJ*, **848**, L12
 Anderson J. P., James P. A., 2008, *MNRAS*, **390**, 1527
 Anderson J. P., James P. A., 2009, *MNRAS*, **399**, 559
 Anderson J. P., Haberman S. M., James P. A., Hamuy M., 2012a, *MNRAS*, **424**, 1372
 Anderson L. D., Bania T. M., Balser D. S., Rood R. T., 2012b, *ApJ*, **754**, 62
 Anderson J. P., James P. A., Haberman S. M., Galbany L., Kuncarayakti H., 2015a, *Publ. Astron. Soc. Australia*, **32**, e019

⁴ <https://www.astropy.org>

- Anderson J. P., James P. A., Förster F., González-Gaitán S., Habbergham S. M., Hamuy M., Lyman J. D., 2015b, *MNRAS*, **448**, 732
- Arnason R. M., Papei H., Barmby P., Bahramian A., Gorski M. D., 2021, arXiv e-prints, p. [arXiv:2102.02615](https://arxiv.org/abs/2102.02615)
- Astropy Collaboration et al., 2013, *A&A*, **558**, A33
- Audcent-Ross F. M., Meurer G. R., Audcent J. R., Ryder S. D., Wong O. I., Phan J., Williamson A., Kim J. H., 2020, *MNRAS*, **492**, 848
- Bailes M., et al., 2021, *MNRAS*,
- Baring M. G., Wadiasingh Z., Gonthier P. L., Harding A. K., Hu K., 2020, arXiv e-prints, p. [arXiv:2012.10815](https://arxiv.org/abs/2012.10815)
- Barthelmy S. D., et al., 2005, *Nature*, **438**, 994
- Bassa C. G., et al., 2017, *ApJ*, **843**, L8
- Beniamini P., Hotokezaka K., van der Horst A., Kouveliotou C., 2019, *MNRAS*, **487**, 1426
- Beniamini P., Wadiasingh Z., Metzger B. D., 2020, *MNRAS*, **496**, 3390
- Bhandari S., et al., 2020, *ApJ*, **895**, L37
- Bhardwaj M., et al., 2021, arXiv e-prints, p. [arXiv:2103.01295](https://arxiv.org/abs/2103.01295)
- Binney J., Gerhard O., Spergel D., 1997, *MNRAS*, **288**, 365
- Blanchard P. K., Berger E., Fong W.-f., 2016, *ApJ*, **817**, 144
- Bland-Hawthorn J., Gerhard O., 2016, *ARA&A*, **54**, 529
- Boardman N., et al., 2020, *MNRAS*, **498**, 4943
- Bochenek C. D., Ravi V., Dong D., 2020a, arXiv e-prints, p. [arXiv:2009.13030](https://arxiv.org/abs/2009.13030)
- Bochenek C. D., Ravi V., Belov K. V., Hallinan G., Kocz J., Kulkarni S. R., McKenna D. L., 2020b, *Nature*, **587**, 59
- Bodaghee A., et al., 2007, *A&A*, **467**, 585
- Bodaghee A., Tomsick J. A., Rodriguez J., James J. B., 2012, *ApJ*, **744**, 108
- Boissier S., Prantzos N., 1999, *MNRAS*, **307**, 857
- Brunthaler A., et al., 2011, *Astronomische Nachrichten*, **332**, 461
- Burns E., et al., 2021, arXiv e-prints, p. [arXiv:2101.05144](https://arxiv.org/abs/2101.05144)
- CHIME/FRB Collaboration et al., 2020, *Nature*, **587**, 54
- Cameron E., Driver S. P., Graham A. W., Liske J., 2009, *ApJ*, **699**, 105
- Castrillo A., et al., 2021, *MNRAS*, **501**, 3122
- Chatterjee S., 2020, arXiv e-prints, p. [arXiv:2012.10377](https://arxiv.org/abs/2012.10377)
- Chen B. Q., et al., 2017, *MNRAS*, **464**, 2545
- Chittidi J. S., et al., 2020, arXiv e-prints, p. [arXiv:2005.13158](https://arxiv.org/abs/2005.13158)
- Church R. P., Levan A. J., Davies M. B., Tanvir N., 2011, *MNRAS*, **413**, 2004
- Churchwell E., et al., 2009, *PASP*, **121**, 213
- Coleiro A., Chaty S., 2013, *ApJ*, **764**, 185
- Coleiro A., Chaty S., Zurita Heras J. A., Rahoui F., Tomsick J. A., 2013, *A&A*, **560**, A108
- Colina L., García Vargas M. L., Mas-Hesse J. M., Alberdi A., Krabbe A., 1997, *ApJ*, **484**, L41
- Collazzi A. C., et al., 2015, *ApJS*, **218**, 11
- Cordes J. M., Lazio T. J. W., 2002, arXiv e-prints, p. [astro-ph/0207156](https://arxiv.org/abs/astro-ph/0207156)
- Crowther P. A., 2013, *MNRAS*, **428**, 1927
- De K., et al., 2020a, *ApJ*, **901**, L7
- De K., et al., 2020b, *ApJ*, **905**, 58
- Díaz-García S., Salo H., Knapen J. H., Herrera-Endoqui M., 2019, *A&A*, **631**, A94
- Duncan R. C., Thompson C., 1992, *ApJ*, **392**, L9
- Eftekhari T., Berger E., 2017, *ApJ*, **849**, 162
- Eldridge J. J., Langer N., Tout C. A., 2011, *MNRAS*, **414**, 3501
- Fahlman G. G., Gregory P. C., 1981, *Nature*, **293**, 202
- Flynn C., Holmberg J., Portinari L., Fuchs B., Jahreiß H., 2006, *MNRAS*, **372**, 1149
- Fong W., Berger E., Fox D. B., 2010, *ApJ*, **708**, 9
- Fong W., et al., 2013, *ApJ*, **769**, 56
- Fraser-McKelvie A., Merrifield M., Aragón-Salamanca A., 2019, *MNRAS*, **489**, 5030
- Fruchter A. S., et al., 2006, *Nature*, **441**, 463
- Gaia Collaboration et al., 2016, *A&A*, **595**, A1
- Gardenier D. W., van Leeuwen J., 2020, arXiv e-prints, p. [arXiv:2012.06396](https://arxiv.org/abs/2012.06396)
- Gorski M., Ott J., Rand R., Meier D. S., Momjian E., Schinnerer E., 2018, *ApJ*, **856**, 134
- Grady J., Belokurov V., Evans N. W., 2020, *MNRAS*, **492**, 3128
- Gravity Collaboration et al., 2019, *A&A*, **625**, L10
- Green J. A., et al., 2017, *MNRAS*, **469**, 1383
- Harris C. R., et al., 2020, arXiv e-prints, p. [arXiv:2006.10256](https://arxiv.org/abs/2006.10256)
- Heintz K. E., et al., 2020, *ApJ*, **903**, 152
- Hilmarsson G. H., et al., 2020, *MNRAS*, **493**, 5170
- Hobbs G., Lorimer D. R., Lyne A. G., Kramer M., 2005, *MNRAS*, **360**, 974
- Hunter J. D., 2007, *Computing in Science and Engineering*, **9**, 90
- Hurley K., et al., 2005, *Nature*, **434**, 1098
- Ioka K., Zhang B., 2020, *ApJ*, **893**, L26
- James P. A., Anderson J. P., 2006, *A&A*, **453**, 57
- James C. W., Prochaska J. X., Macquart J. P., North-Hickey F., Bannister K. W., Dunning A., 2021, arXiv e-prints, p. [arXiv:2101.08005](https://arxiv.org/abs/2101.08005)
- Jonker P. G., Nelemans G., 2004, *MNRAS*, **354**, 355
- Kasen D., Bildsten L., 2010, *ApJ*, **717**, 245
- Katz J. I., 2016, *ApJ*, **826**, 226
- Keane E. F., 2018, *Nature Astronomy*, **2**, 865
- Kelly P. L., Kirshner R. P., 2012, *ApJ*, **759**, 107
- Kouveliotou C., et al., 1998, *Nature*, **393**, 235
- Kretschmar P., et al., 2019, *New Astron. Rev.*, **86**, 101546
- Krivonos R. A., Tsygankov S. S., Mereminskiy I. A., Lutovinov A. A., Sazonov S. Y., Sunyaev R. A., 2017, *MNRAS*, **470**, 512
- Kumar R., Pradhan A. C., Ojha D. K., Piridi S., Baug T., Ghosh S. K., 2020, arXiv e-prints, p. [arXiv:2012.09526](https://arxiv.org/abs/2012.09526)
- Lee J. C., et al., 2021, arXiv e-prints, p. [arXiv:2101.02855](https://arxiv.org/abs/2101.02855)
- Li D., Zanazzi J. J., 2021, arXiv e-prints, p. [arXiv:2101.05836](https://arxiv.org/abs/2101.05836)
- Li Y., Zhang B., 2020, *ApJ*, **899**, L6
- Li C. K., et al., 2021, *Nature Astronomy*,
- Licquia T. C., Newman J. A., Brinchmann J., 2015, *ApJ*, **809**, 96
- Lim D., et al., 2021, arXiv e-prints, p. [arXiv:2101.06269](https://arxiv.org/abs/2101.06269)
- Lin L., et al., 2020, *Nature*, **587**, 63
- Lumsden S. L., Hoare M. G., Urquhart J. S., Oudmaijer R. D., Davies B., Mottram J. C., Cooper H. D. B., Moore T. J. T., 2013, *ApJS*, **208**, 11
- Lunnan R., et al., 2015, *ApJ*, **804**, 90
- Lunnan R., et al., 2017, *ApJ*, **836**, 60
- Luo R., Men Y., Lee K., Wang W., Lorimer D. R., Zhang B., 2020, *MNRAS*, **494**, 665
- Lyman J. D., et al., 2017, *MNRAS*, **467**, 1795
- Lyutikov M., Toonen S., 2019, *MNRAS*, **487**, 5618
- Manchester R. N., Hobbs G. B., Teoh A., Hobbs M., 2005, *AJ*, **129**, 1993
- Manchester R. N., Hobbs G. B., Teoh A., Hobbs M., 2016, *VizieR Online Data Catalog*, p. [B/psr](https://vizier.cesr-lab.fr/vizie1/planck/psr/)
- Mannings A. G., et al., 2020, arXiv e-prints, p. [arXiv:2012.11617](https://arxiv.org/abs/2012.11617)
- Margalit B., Berger E., Metzger B. D., 2019, *ApJ*, **886**, 110
- Margalit B., Beniamini P., Sridhar N., Metzger B. D., 2020, *ApJ*, **899**, L27
- Mazets E. P., Golenetskij S. V., Guryan Y. A., 1979a, *Soviet Astronomy Letters*, **5**, 343
- Mazets E. P., Golenskii S. V., Ilinskii V. N., Aptekar R. L., Guryan I. A., 1979b, *Nature*, **282**, 587
- McMillan P. J., 2011, *MNRAS*, **414**, 2446
- Metzger B. D., Quataert E., Thompson T. A., 2008, *MNRAS*, **385**, 1455
- Metzger B. D., Giannios D., Thompson T. A., Bucciantini N., Quataert E., 2011, *MNRAS*, **413**, 2031
- Metzger B. D., Berger E., Margalit B., 2017, *ApJ*, **841**, 14
- Mondal S., Bera A., Chandra P., Das B., 2020, *MNRAS*, **498**, 3863
- Núñez C., et al., 2021, arXiv e-prints, p. [arXiv:2104.09727](https://arxiv.org/abs/2104.09727)
- Ofek E. O., et al., 2006, *ApJ*, **652**, 507
- Ofek E. O., et al., 2008, *ApJ*, **681**, 1464
- Olausen S. A., Kaspi V. M., 2014, *ApJS*, **212**, 6
- Palliyaguru N. T., Agarwal D., Golpayegani G., Lynch R., Lorimer D. R., Nguyen B., Corsi A., Burke-Spolaor S., 2021, *MNRAS*, **501**, 541
- Perets H. B., Beniamini P., 2021, arXiv e-prints, p. [arXiv:2101.11622](https://arxiv.org/abs/2101.11622)
- Perez F., Granger B. E., 2007, *Computing in Science and Engineering*, **9**, 21
- Pestalozzi M. R., Minier V., Booth R. S., 2005, *A&A*, **432**, 737
- Platts E., Weltman A., Walters A., Tendulkar S. P., Gordin J. E. B., Kandhai S., 2019, *Phys. Rep.*, **821**, 1
- Price-Whelan A. M., et al., 2018, *AJ*, **156**, 123
- Rajwade K. M., Lorimer D. R., Anderson L. D., 2017, *MNRAS*, **471**, 730
- Reid M. J., et al., 2014, *ApJ*, **783**, 130
- Reid M. J., Dame T. M., Menten K. M., Brunthaler A., 2016, *ApJ*, **823**, 77
- Reid M. J., et al., 2019, *ApJ*, **885**, 131

Repetto S., Igoshev A. P., Nelemans G., 2017, *MNRAS*, **467**, 298
 Rich R. M., et al., 2020, *MNRAS*, **499**, 2340
 Ridnaia A., et al., 2021, *Nature Astronomy*,
 Roberts W. W., 1969, *ApJ*, **158**, 123
 Russeil D., 2003, *A&A*, **397**, 133
 Safarzadeh M., Prochaska J. X., Heintz K. E., Fong W.-f., 2020, *ApJ*, **905**,
 L30
 Sartore N., Ripamonti E., Treves A., Turolla R., 2010, *A&A*, **510**, A23
 Sazonov S., et al., 2020, *New Astron. Rev.*, **88**, 101536
 Schulze S., et al., 2020, arXiv e-prints, p. arXiv:2008.05988
 Schweizer F., 1976, *ApJS*, **31**, 313
 Seigar M. S., James P. A., 1998, *MNRAS*, **299**, 685
 Sharma S., Bland-Hawthorn J., Johnston K. V., Binney J., 2011, *ApJ*, **730**, 3
 Siegel M. H., Majewski S. R., Reid I. N., Thompson I. B., 2002, *ApJ*, **578**,
 151
 Sridhar N., Metzger B. D., Beniamini P., Margalit B., Renzo M., Sironi L.,
 2021, arXiv e-prints, p. arXiv:2102.06138
 Svensson K. M., Levan A. J., Tanvir N. R., Fruchter A. S., Strolger L. G.,
 2010, *MNRAS*, **405**, 57
 Svinkin D., et al., 2021, arXiv e-prints, p. arXiv:2101.05104
 Tavani M., et al., 2021, *Nature Astronomy*,
 Tendulkar S. P., Cameron P. B., Kulkarni S. R., 2013, *ApJ*, **772**, 31
 Tendulkar S. P., et al., 2021, *ApJ*, **908**, L12
 Thompson C., Duncan R. C., 1996, *ApJ*, **473**, 322
 Tunncliffe R. L., et al., 2014, *MNRAS*, **437**, 1495
 Uddin S. A., et al., 2020, *ApJ*, **901**, 143
 Urquhart J. S., Figura C. C., Moore T. J. T., Hoare M. G., Lumsden S. L.,
 Mottram J. C., Thompson M. A., Oudmaijer R. D., 2014, *MNRAS*, **437**,
 1791
 Valdetaro R., et al., 2001, *A&A*, **368**, 845
 Vallée J. P., 2002, *ApJ*, **566**, 261
 Vallée J. P., 2008, *AJ*, **135**, 1301
 Verberne S., Vink J., 2021, arXiv e-prints, p. arXiv:2103.16973
 Verrecchia F., et al., 2021, arXiv e-prints, p. arXiv:2105.00685
 Virtanen P., et al., 2020, *Nature Methods*, **17**, 261
 Wang X., Wang L., Filippenko A. V., Zhang T., Zhao X., 2013, *Science*, **340**,
 170
 White N. E., van Paradijs J., 1996, *ApJ*, **473**, L25
 Widrow L. M., Pym B., Dubinski J., 2008, *ApJ*, **679**, 1239
 Winkler C., et al., 2003, *A&A*, **411**, L1
 Wisnioski E., Glazebrook K., Blake C., Poole G. B., Green A. W., Wyder T.,
 Martin C., 2012, *MNRAS*, **422**, 3339
 Woosley S. E., 2010, *ApJ*, **719**, L204
 Wright E. L., 2006, *PASP*, **118**, 1711
 Xiao D., Wang F., Dai Z., 2021, arXiv e-prints, p. arXiv:2101.04907
 Yao J. M., Manchester R. N., Wang N., 2017, *ApJ*, **835**, 29
 Yu S.-Y., Ho L. C., 2020, *ApJ*, **900**, 150
 Yu S.-Y., Ho L. C., Barth A. J., Li Z.-Y., 2018, *ApJ*, **862**, 13
 Zhang B., 2020, *Nature*, **587**, 45
 Zhao Z. Y., Zhang G. Q., Wang Y. Y., Tu Z.-L., Wang F. Y., 2021, *ApJ*, **907**,
 111
 van Paradijs J., White N., 1995, *ApJ*, **447**, L33

<https://github.com/achrimes2/MW-NS-Flight> or as supplementary materials on the journal website, along with the equivalent data for pulsars and XRBS.

This paper has been typeset from a $\text{\TeX}/\text{\LaTeX}$ file prepared by the author.

APPENDIX A: MILKY WAY MAGNETAR MEASUREMENTS

In Table A1 of this appendix, we provide a table of measurements for the 20 Milky Way magnetars which lie this side of Galactic centre ($y < 8.3$ kpc on our map). The measurements are typical of those used in extragalactic transient studies, including host offset, host normalised offset, F_{light} and the enclosed flux fraction at their radius. The heliocentric distances, their uncertainties, the type of measurement, are also provided (reproduced from the McGill magnetar catalogue, Olausen & Kaspi 2014). The results can be used in future comparative studies, and are available at

Table A1. The 20 magnetars that satisfy the criteria of having (i) a distance estimate, (ii) lying at $y < 8.3$ kpc. Magnetar distance information is from the McGill catalogue (Olausen & Kaspi 2014, and reference therein). The F_{light} values are calculated using a 12 kpc pixel selection radius and pixels from the whole Galaxy.

Magnetar	Dist./Assoc.	d_{\odot} [kpc]	δr [kpc]	$\delta r/r_e$ (B)	$\delta r/r_e$ (I)	F_{light} (B)	F_{light} (I)	F_{enc} (B)	F_{enc} (I)
4U0142+61	RC	$3.6^{+0.4}_{-0.4}$	10.85	2.89	3.31	0.03	0.03	0.96	0.96
SGR0418+5729	PA	~2	9.95	2.65	3.03	0.12	0.10	0.93	0.92
SGR0501+4516	PA/SNR	~2	10.12	2.7	3.08	0.06	0.06	0.93	0.93
1E1048.1-5937	RC	$9^{+1.7}_{-1.7}$	10.10	2.69	3.08	0.06	0.06	0.94	0.93
1E1547.0-5408	SNR	$4.5^{+0.5}_{-0.5}$	5.04	1.34	1.54	0.44	0.39	0.44	0.54
PSRJ1622-4950	DM/SNR	$9^{+1.4}_{-1.4}$	3.97	1.06	1.21	0.44	0.41	0.29	0.43
CXOUJ164710.2-455216	CA	$3.9^{+0.7}_{-0.7}$	4.75	1.27	1.45	0.41	0.38	0.39	0.52
1RXSJ170849.0-400910	RC	$3.8^{+0.5}_{-0.5}$	4.59	1.22	1.4	0.44	0.40	0.37	0.50
SGRJ1745-2900	HI	$8.3^{+0.3}_{-0.3}$	0.10	0.03	0.03	0.99	0.99	0.00	0.00
XTEJ1810-197	HI	$3.5^{+0.3}_{-0.4}$	4.81	1.28	1.47	0.49	0.43	0.39	0.52
SwiftJ1818.0-1607	DM	$4.8^{+1.65}_{-1.65}$	3.77	1	1.15	0.53	0.53	0.27	0.41
SwiftJ1822.3-1606	HI/HII	$1.6^{+0.3}_{-0.3}$	6.67	1.78	2.03	0.71	0.57	0.65	0.69
SwiftJ1834.9-0846	SNR	$4.2^{+0.3}_{-0.3}$	4.65	1.24	1.42	0.86	0.72	0.37	0.50
1E1841-045	SNR	$8.5^{+1.3}_{-1}$	3.96	1.06	1.21	0.64	0.53	0.27	0.41
3XMMJ185246.6+003317	HI/SNR	~7.1	4.54	1.21	1.39	0.44	0.40	0.33	0.47
SGR1935+2154	F/SNR	$6.5^{+3.0}_{-5.3}$	7.20	1.92	2.19	0.20	0.19	0.69	0.73
1E2259+586	SNR/PA	$3.2^{+0.2}_{-0.2}$	9.73	2.59	2.97	0.24	0.19	0.91	0.91
AXJ1845.0-0258	HI/SNR	~8.5	4.27	1.14	1.3	0.64	0.53	0.3	0.44
SGR2013+34	HII	~8.8	10.04	2.68	3.06	0.06	0.06	0.92	0.92
PSRJ1846-0258	SNR	$6^{+1.5}_{-0.9}$	4.22	1.12	1.29	0.49	0.46	0.3	0.44

RC - distance from red clump stars, PA - Perseus arm association, SNR - supernova remnant association, DM - dispersion measure distance, CA - cluster association, HI - distance from HI column density, HII - HII region association, F - distance estimate from burst flux